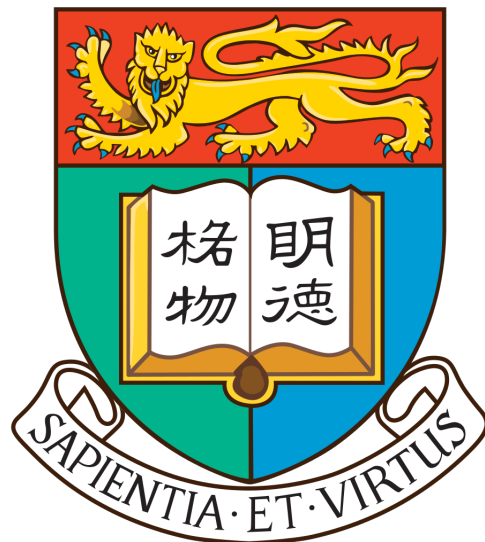


# Thesis Title

Department of Physics, The University of Hong Kong, Pokfulam Road,  
Hong Kong



Wang WenChao  
3030053350

---

# Contents

<b>1</b>	<b>Introduction</b>	<b>1</b>
1.1	Neutron Stars and Pulsars . . . . .	1
1.2	Emission Mechanism of Pulsars . . . . .	1
1.2.1	Magnetic Dipole Model . . . . .	2
1.2.2	A More Sophisticated Model . . . . .	2
1.3	Millisecond Pulsar . . . . .	3
1.3.1	P- $\dot{P}$ Diagram . . . . .	3
1.3.2	Origin Of Millisecond Pulsars . . . . .	4
1.3.3	Class II MSPs . . . . .	5
1.4	Objectives . . . . .	6
1.5	NuSTAR . . . . .	6
1.5.1	Detectors . . . . .	6
1.5.2	Optics . . . . .	7
1.5.3	Mast . . . . .	7
1.5.4	Performance of NuSTAR . . . . .	8
1.6	The Procedures of Processing NuSTAR Data . . . . .	9
1.6.1	Data Calibration . . . . .	10
1.6.2	Data Screening . . . . .	11
1.6.3	Products Extraction . . . . .	11
<b>2</b>	<b>Data Analysis</b>	<b>13</b>

2.1	Data Analysis of Pulsar B1937+21 Using NuSTAR . . . . .	13
<b>3</b>	<b>Gamma-Ray Analysis</b>	<b>21</b>
3.1	Gamma-Ray Emission Mechanism of MSPs . . . . .	21
3.1.1	synchrotron radiation . . . . .	21
3.1.2	Curvature Radiation . . . . .	23
3.1.3	Inverse-Compton radiation . . . . .	23
3.1.4	Two-layer Model . . . . .	24
3.2	Introduction of The Fermi Gamma-ray Space Telescope . . . . .	26
3.3	Analysis With Fermi LAT . . . . .	27
3.3.1	PSR J0218+4232 . . . . .	28
3.3.2	PSR J1824.6-2452 . . . . .	32
3.3.3	PSR J1939+2134 . . . . .	35

## **Abstract**

Recent observations find that some millisecond pulsars (known as Class II MSPs) show aligned pulse profiles in different energy bands. Conventionally, radio and gamma-ray emission are produced in different regions—in polar cap and outer gap respectively. The finding of Class II MSPs implies that radio, X-ray and gamma-ray emission can all be emitted in outer gap. This means that Class II MSPs can have a different emission mechanism. Recently, scientists propose a model suggesting that hard X-ray can be emitted by inverse Compton scattering between radio waves and energetic charged particles. The objective of the thesis is to test this model by measuring hard X-ray spectra of some Class II MSPs using *NuSTAR*.

# *Chapter 1*

---

## **Introduction**

### **1.1 Neutron Stars and Pulsars**

Neutron stars are produced by a supernova explosion of massive stars which have about 4 to 8 solar mass. After the supernova explosion, the star leaves a central region. And the central region collapses because of the effect of gravity until protons and electrons combine to form neutrons ( $e^- + p \rightarrow n + \nu_e$ ) —the reason why they are called “neutron stars”. Because neutrons have no electromagnetic force on each other, they can be squeezed very tightly. Therefore, a neutron star has tremendous high density (about  $5 \times 10^{17} kg/m^3$ ) and its diameter and mass is about 20km and 1.4 solar mass respectively. What prevents a neutron star to continue to contract is the degeneracy pressure of neutrons.

Pulsars are fast-spinning neutron stars. Their rotational periods can be from a few milliseconds to several seconds. For example, the rotational period of PSR B1937+21 is about  $1.56ms$  while PSR B1919+21 is approximately  $1.34s$ . As we know, a star can be ripped by centrifugal force if the star rotates too fast. We can estimate lower limit of density of a star with the equation:  $\rho = \frac{3\pi}{P^2 G}$ , where  $P$  is the rotational period of a pulsar. Just for simplicity, we let  $P$  be  $1s$ . Then we get  $\rho \approx 1.4 \times 10^{11} kg/m^3$ . With the knowledge that the density of a white dwarf is about  $1 \times 10^9 kg/m^3$  which is smaller than the lower density limit, the observed fast-spinning stars belong to the kind of stars which are much denser than white dwarf. As a result, neutron stars are ideal candidates for pulsars.

More than 2000 pulsars have been found so far. Most of them are in the disk of our Galaxy while we also can find a small portion of them in high latitude, which can be seen clearly in the figure 1.1. This may because they cannot escape the gravitational potential if their kinetic energy is not large enough. Besides, even though they have large enough velocities to escape from their birth region, there are some probabilities that they become nearly non-detectable before reaching high latitude.

### **1.2 Emission Mechanism of Pulsars**

Although emission mechanism of pulsars has not been fully understood yet, some models are developed trying to explain observational facts. The following is one toy model that can explain some basic features of pulsars.

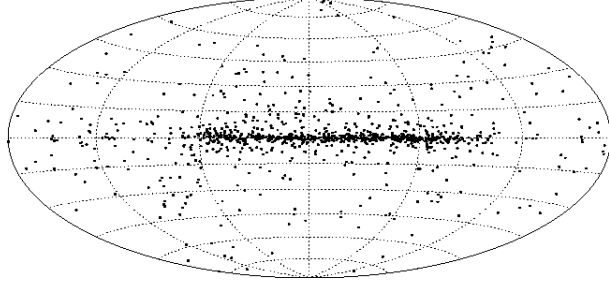


**Figure 1.1:** Spatial distribution of some pulsars in galactic coordinate system.

### 1.2.1 Magnetic Dipole Model

Assume a pulsar has a magnetic dipole moment  $\vec{m}$ , the angle between rotation axis and direction of  $\vec{m}$  is  $\alpha$ , its angular velocity is  $\Omega$ , radius is  $R$  and moment of inertia is  $I$ . Also by assuming that energy of electromagnetic radiation are all from rotational energy, its spin-down rate can be written as:

$$\dot{\Omega} = -\frac{B_p^2 R^6 \Omega^3 \sin \alpha^3}{6c^3 I}$$

where  $B_p$  is magnetic field strength in the pole of the pulsar. Its surface magnetic field can also be estimated by:

$$B_s = \sqrt{\frac{3c^3 I}{2\pi^2 R^6}} P \dot{P} = 3.2 \times 10^{19} \sqrt{P \dot{P}}$$

where  $B_s$  is the strength of surface magnetic field.

In general, a pulsar's spin down rate can be expressed as:  $\dot{\Omega} = -K\Omega^n$ , where  $K$  is a constant and  $n$  is called braking index. In magnetic dipole model  $n$  is 3 ([H.Tong 2015](#)). Then characteristic age of the pulsar can be defined as:  $P/2\dot{P}$  in magnetic dipole model. For example, the Crab pulsar's rotation period is about 0.033s and period derivative is  $4.22 \times 10^{-13} \text{ s/s}$ . The characteristic age is about 1200 years. The pulsar is remnant of a supernova which is observed by ancient astronomers in 1054 AD, so the record shows that characteristic age can give us order of magnitude estimate of a pulsar's real age.

Although braking index is 3 in magnetic dipole model, most of pulsars' braking index is less than 3 as shown in figure 1.2. The reason is that if a pulsar's spin down is completely because of pulsar wind, the braking index is 1. Thus, the real braking index should be a combination of 1 and 3, which is usually less than 3 ([Oliver Hamil 2014](#)).

### 1.2.2 A More Sophisticated Model

It is oversimplified to regard a pulsar as a magnetized sphere rotating in vacuum. Actually, there are plenty of charged particles in a pulsar's magnetosphere which co-rotate with the pulsar. The creation of charged particles can be described by the following steps ([P.A.Sturrock 1971](#)).

1. The co-rotating charged primary particles emit gamma-ray by curvature radiation because of acceleration in super strong magnetic field.
2. In super intense magnetic field, the high energy photons decay into electrons and positrons which are called secondary particles by the process:  $\gamma + (B) \rightarrow e^+ + e^- + (B)$ . Synchrotron photons can be emitted by these secondary particles.

Pulsar	$n_{\text{obs}}$	$\Omega$ $\text{s}^{-1}$	$\dot{\Omega}$ $10^{-10}\text{s}^{-2}$
PSR B0531+21 (Crab)	$2.51 \pm 0.01$	$30.22543701$	$-3.862283$
PSR B0540-69	$2.14 \pm 0.01$	$19.8344965$	$-1.88383$
PSR B0833-45 (Vela)	$1.4 \pm 0.2$	$11.2$	$-0.157$
PSR B1509-58	$2.839 \pm 0.001$	$6.633598804$	$-0.675801754$
PSR J1846-0258	$2.16 \pm 0.13$	$3.0621185502$	$-0.6664350$
PSR J1833-1034	$1.857 \pm 0.001$	$16.159357$	$-0.5275017$
PSR J1119-6127	$2.684 \pm 0.001$	$2.4512027814$	$0.2415507$
PSR J1734-3333	$0.9 \pm 0.2$	$0.855182765$	$-0.0166702$

**Figure 1.2:** Braking index of some pulsars.

3. Secondary particles are also accelerated in strong magnetic field which is just like primary particles. As a result, these charged particles can create more secondary particles.

This chain of process is quite efficient to produce charged particles and pulsar's magnetosphere is filled with plasma as a consequence. So, it is natural to think of the distribution of charges in pulsar's magnetosphere. A characteristic charge density  $\rho_{GJ} = -\frac{\vec{\Omega} \cdot \vec{B}}{2\pi c}$  is called Goldreich-Julian density. This charges can offset part of electric field ( $E_{||}$ ) which is parallel to magnetic field. There is some region in the magnetosphere called "outer gap" where  $\rho_{GJ}$  is so small that it can't screen  $E_{||}$  effectively. As a result, the secondary particles can be accelerated at a very large velocity (Lorentz factor  $\gamma \sim 10^7$ ) and emit gamma-ray. Photons in outer gap can also create electrons and positrons by the process:  $\gamma + \gamma \rightarrow e^- + e^+$ . At the outer gap, one-photon pair production can't happen because magnetic field is too weak in this region.

## 1.3 Millisecond Pulsar

### 1.3.1 P- $\dot{P}$ Diagram

P- $\dot{P}$  diagram is an important tool for analyzing evolution of pulsars. Period (P) and time derivative of period ( $\dot{P}$ ) are two of pulsars' important characteristics. Analyzing the position of a pulsar in P- $\dot{P}$  diagram can give some valuable information such as which evolution stage the pulsar is in or the type of the pulsar, etc. The figure 1.3 is an example of P- $\dot{P}$  diagram. The horizontal axis is pulsars' rotation periods and the vertical axis is time derivative of rotation periods. In this P- $\dot{P}$  diagram, the negative slope lines represent the strength of surface magnetic field while the positive slope lines represent the characteristic age of pulsars. The following is a short explanation for this. From previous discussion, we have known that the characteristic age of a pulsar is  $\tau = -P/\dot{P} = P/(-\dot{P})$ , so line of constant  $\tau$  is a set of straight lines with equal positive slope. We also know  $B \propto \sqrt{P\dot{P}}$ , therefore the line of constant  $B$  should be a part of hyperbola. When  $\dot{P}$  is very small, the hyperbola looks like a straight line with negative slope.

This figure shows that most pulsars lie in the position about  $1\text{s}, 10^{-14}\text{s/s}$ . At the same time, a couple of stars lie at the bottom-left of the figure—these are millisecond pulsars (MSP). Their rotation periods are about 1-20 milliseconds. It is believed that MSPs are

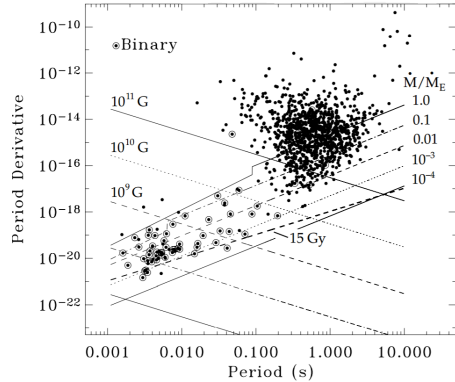


**Figure 1.3:** Position of pulsars in  $P-\dot{P}$  diagram

spun up by accretion of mass from its companion star. In the above  $P-\dot{P}$  diagram, we can observe that millisecond pulsars' surface magnetic field are about 3 to 4 orders of magnitude lower than those of normal pulsars. However, an MSP has a relative strong magnetic field near its light cylinder. The reason is that an MSP's radius of light cylinder ( $R_{lc} = c/\omega$ ) is much smaller than a normal pulsar's because of its short rotation period and the magnetic field near light cylinder can be estimated as  $B_{lc} \sim (R/R_{lc})^3$ . At the same time, pulsars' emission mechanism is closely related to their magnetic field near light cylinder. As a result, like a normal pulsar, an MSP also have broadband spectrum from radio to gamma rays.

### 1.3.2 Origin Of Millisecond Pulsars

From pulsars' emission mechanism, we know that magnetic field of a pulsar decreases with time while the spin period increase with time. But MSPs' spin period is much shorter than normal pulsars and surface magnetic field is a lot weaker. This makes an MSP seem to be both young and old. As a result, people think millisecond pulsars are old pulsars spun up by its companion. The companion star transfer mass and angular momentum to accelerate the pulsar. Therefore, the aged pulsar can spin faster gradually.

### Mass Transfer And Accretion In Binary Systems

X-ray binaries are a type of binary systems that is luminous in X-ray band. There are several kinds of X-ray binaries including low mass X-ray binaries (LMXB) and high mass X-ray binaries (HMXB). The way of transferring mass is different in these two types of systems. Before discussing mass transfer, we need to know a little bit about Roche Lobe. The figure 1.4 is a schematic diagram of Roche lobe.

We call two stars in an LMXB as A and B respectively for convenience. It is obvious that if an object is close to star A, the gravitational influence of A is so strong that we can nearly ignore the effect of star B. Similarly, this is true for star B. As a result, there must be a point where the effect of star A is equal to star B which is called inner Lagrange point ([Seidov 2013](#)). The two volumes inside the largest equipotential lines of A and B are called Roche lobe. If star B cross its Roche lobe, than its mass will be attracted by A thus mass transfer between A and B happens. We should notice that this is the main way of mass transfer in LMXB. While in HMXB, the mass can be transferred by strong wind of the massive companion star.

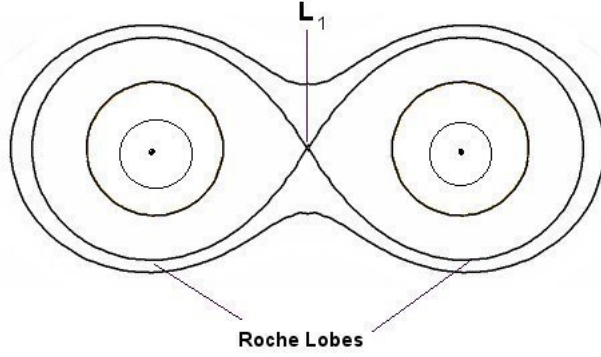


**Figure 1.4:** Schematic diagram of Roche lobe.  $L_1$  is called inner Lagrange point which is the intersection of equipotential lines of star A and B.

What should be noted is that mass transfer can change the distance between two companion stars. If low-mass star transfer mass to high-mass companion star, the orbital separation will be large. This can actually stop mass transfer and is like negative feedback. On the contrary, mass transfer from high-mass star to low-mass star will shrink the orbital distance.

### 1.3.3 Class II MSPs

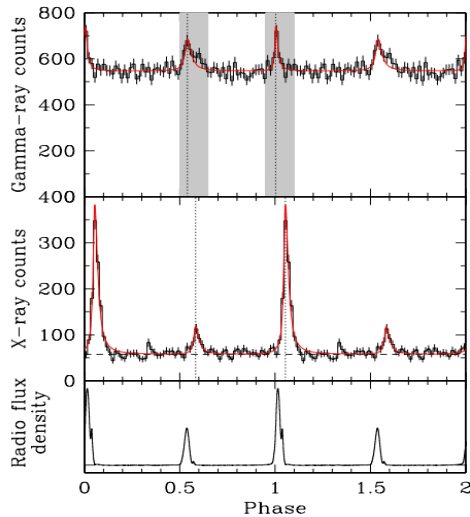


**Figure 1.5:** Pulse profiles of PSR B1937+21 in radio, X-ray and gamma-ray.

Radio emission are usually considered to be emitted above the polar cap, which means radio emission and gamma-ray emission are from different location of pulsar's magnetosphere. However, there are about 10 sources showing aligned pulse profiles in radio and gamma-ray implying that radio emission may produced from outer magnetosphere and they are called Class II MSPs ([Guillemot et al. 2012](#)). These pulsars have strong magnetic field near the light cylinder. The figure 1.5 is an example of aligned pulse profile.

## 1.4 Objectives

Recently, it is found that X-ray band of spectrum of millisecond pulsar B1937+21 has a hard photon index of  $0.9 \pm 0.1$  by analyzing data of *Chandra*, *XMM-Newton* and *Fermi* ([Ng et al. 2014](#)). People think X-ray emission is mainly produced by synchrotron radiation, but it is difficult to explain such a hard photon index. Besides millisecond pulsar B1937+21, it is discovered that hard photon index is a common characteristic of class II MSPs. Therefore, people propose that Inverse Compton scattering can also lead to X-ray emission and build a model recently to explain it ([Ng et al. 2014](#)).

In order to test the model, we need to analyze the hard X-ray band of millisecond pulsars B1937+21, J0218+4232 and B1821-24. The energy ranges of *Chandra* and *XMM-Newton* are up to 10keV and 15keV respectively while *NuSTAR* can be up to 79keV. As a result, we aim to use *NuSTAR* to measure the hard X-ray band of the three MSPs mentioned above.

## 1.5 NuSTAR

*NuSTAR* stands for Nuclear Spectroscopic Telescope Array and is launched in June 12, 2012. It is the first space telescope focusing on hard X-ray (3eV-79eV) band. This is the telescope that we mainly use and it is helpful to know the structure to deal with its data. It mainly composed of three parts: detectors, optics and mast as the figure 1.6 shows.

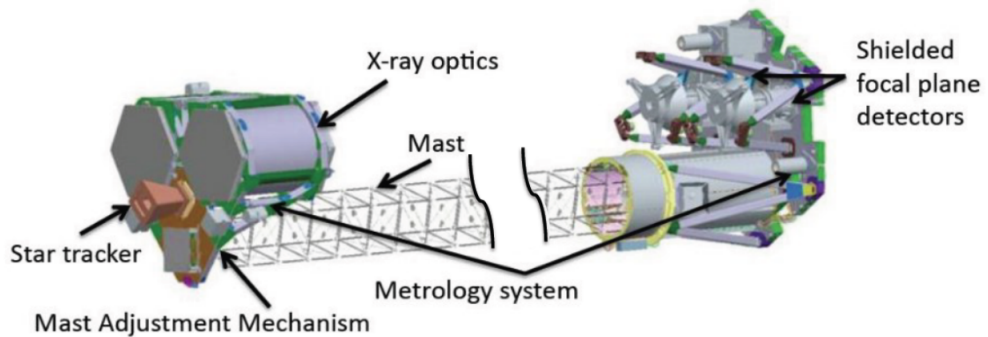


**Figure 1.6:** *NuSTAR's sketch. The mast connects X-ray optics and focal plane detectors.*

### 1.5.1 Detectors

*NuSTAR* has two independent photons counting detector modules (FPMA & FPMB) and each module contains 4 Cadmium-Zinc-Telluride (CZT) detectors. Every detector is a rectangular crystal whose size is  $20mm \times 20mm \times 2mm$  (length  $\times$  width  $\times$  height) and have  $32 \times 32$  pixels.

In order to help to distinguish the source photons and the background photons, the focal planes are shielded with crystals made of Cesium-Iodide (CsI). The CsI shields can record the photons come from directions which are not the direction of *NuSTAR* optical axis. So background photons can be subtracted from the total photon counts.

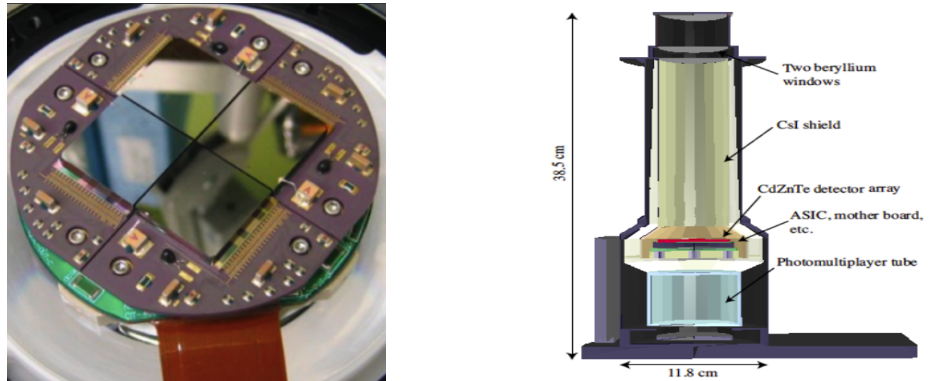


**Figure 1.7:** Left: One of two detector modules which contains  $2 \times 2$  array of independent detectors. Right: One detector module shielded by CsI crystal. CZT detectors can turn high energy photons into electrons very efficiently in room temperature so they are operated at  $15^{\circ}\text{C}$ .

### 1.5.2 Optics

Corresponding to two detector modules, *NuSTAR* also has two optics called Optics Module A and B (OMA & OMB). The focal length is 10.14 meters which is about the same length with its mast. X-ray is very hard to reflect so mirrors are usually made of high density materials such as Pt and W. Past telescopes such as *Chandra* uses these high density materials to reflect low energy X-ray (up to 10eV). However, the efficiency of reflecting high energy X-ray drops drastically. High density contrast between two kinds of materials are needed to overcome this problem. As a result, *NuSTAR*'s mirror is coated with Pt/SiC and W/Si multilayers and can reflect hard X-ray up to 79eV.

Besides high density contrast between two materials, a small incident angle is also required. As the figure 1.8 showing, the focal length may be very long because of the

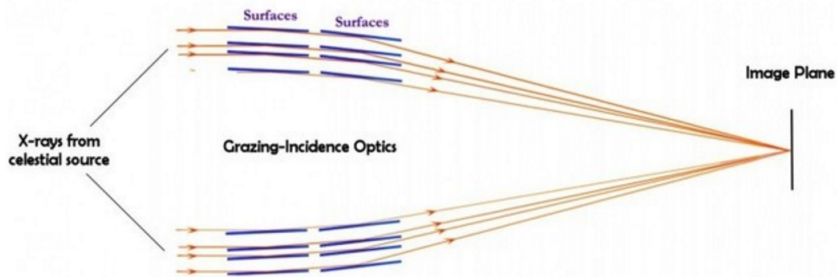


**Figure 1.8:** Light path schematic diagram of reflecting X-ray

small incidence angle. This is partly the reason why *NuSTAR*'s detectors and optics are separated by a 10-meter long mast which will be introduced in the next section.

### 1.5.3 Mast

Although *NuSTAR*'s mast is stable and reliable, it can cause some image distortion because of its deformation. Therefore, careful calibration or measurement of mast's deformation is necessary. In order to achieve this, *NuSTAR* has a laser metrology system which consists of two lasers and two light-sensing detectors. The two lasers are located on optics

while the two detectors are mounted on the detector module. Then, the deformation can be recorded and used to reconstruct the raw data. The figure 1.9 shows what the mast looks like. The reason why *NuSTAR* has a deployable mast is that it is carried by a relative small rockets.

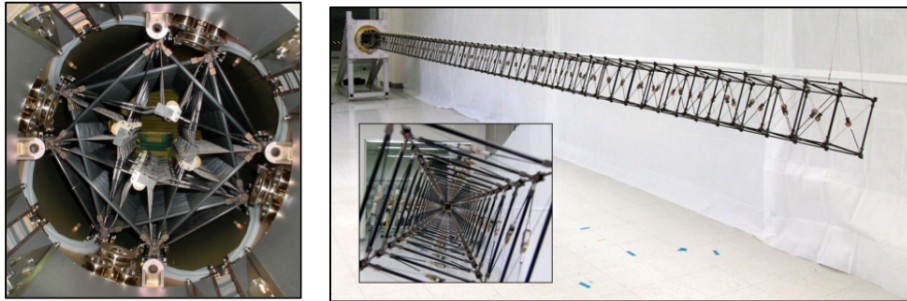


**Figure 1.9:** *NuSTAR*'s mast. Left: stored in container. Right: after being deployed.

#### 1.5.4 Performance of NuSTAR

Though *NuSTAR* has a broad energy range, the effective collecting area at different energy is quite different. The figure 1.10 shows comparison between *NuSTAR* and other telescopes.

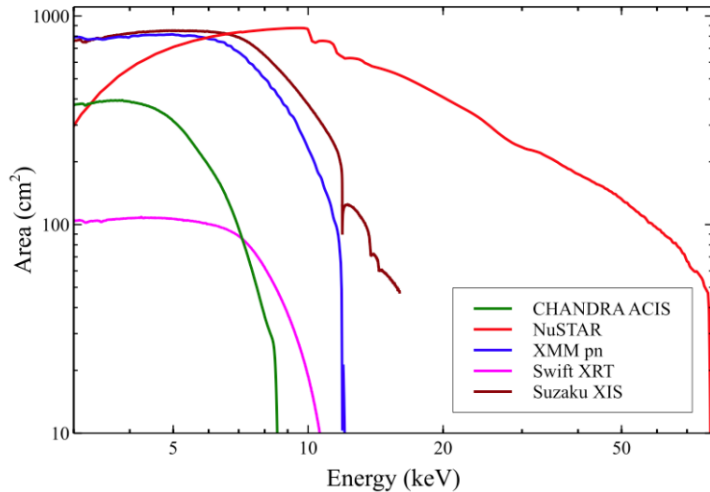


**Figure 1.10:** *NuSTAR*'s effective area compared with other X-ray focusing telescopes.

From figure 1.10 we can see that the effective area drops dramatically after 70keV. Therefore, we may need to screen out the high energy part ( $>70\text{keV}$ ) for data analysis. The figure 1.11 shows the point spread function (PSF) of optics module A and B. In order to make faint pixels look more obvious, the images are in logarithm scale. The PSF of both optics module A and B are dependent on energy. The table 1.12 lists the relationships and from this table we can also see that angular resolution of optics module B is slightly better A.

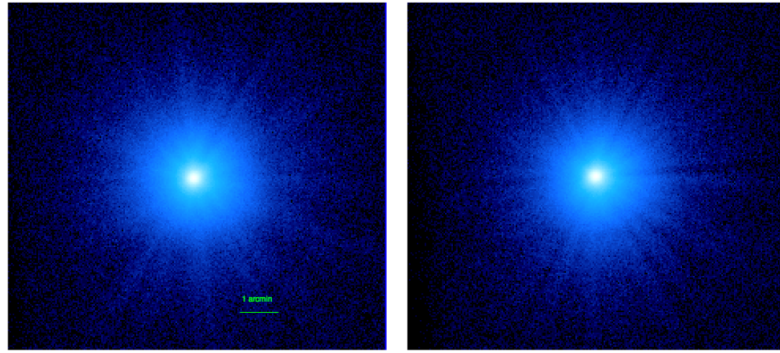


**Figure 1.11:** Image of NuSTAR’s point spread function of optics module A(left) and B(right).

Energy (keV)	FPMA HPD ('')	FPMB HPD ('')
3 – 4.5	70.3	65.6
4.5 – 6	67.1	62.6
6 – 8	64.7	60.7
8 – 12	63.5	59.5
12 – 20	63.4	60.3
20 – 79	63.4	62.4

**Figure 1.12:** PSF (half power diameter) as a function of energy.

## 1.6 The Procedures of Processing NuSTAR Data

*NuSTAR* Data Analysis Software (*NuSTARDAS*) is used for data processing. This includes three steps: data calibration, data screening and products extraction. The next paragraph talks about the reason the first two steps are necessary.

Lots of factors can affect raw data, such as movements of *NuSTAR*’s mast, the orbit of the telescope, etc. As a result, *NuSTAR* data must be calibrated before they can be used to do data analysis. Also, some parts of data are not good for scientific analyzing. For example, there are some bad pixels in the telescope’s detectors which cannot record photons correctly. Thus, the data recorded by these bad pixels have to be treated very carefully. We might get rid of the data when the source is bright, while if the photon counts are too small, we might have to use these data with carefulness. And sometimes we may want to focus on a particular part of data. Thus, we need to screen the calibrated data.

In order to understand data filter process better, it is necessary to know the different levels of *NuSTAR* data. *NuSTAR* data can be divide into 5 levels which is from level 0 to level 3. Level 0 data are raw telemetry files which might not be in formal format (FITS format). Level 1 data contains two parts: level 1 and level 1a. Level 1 data are formatted in FITS format, but not calibrated yet. Level 1a data are level 1 data after calibration. Actually, level 1a data are addition of level 1 data and calibration data. Level 1a data are produced by step 1 (data calibration). Then by step 2 (data screening), we get level 2 data which are cleaned files. We can do data analysis after getting level 2 data. Thus in order to get reliable result, it is key to get raw data properly cleaned. The figure 1.13 is comparison between level 1a event file and level 2 event file after screening.

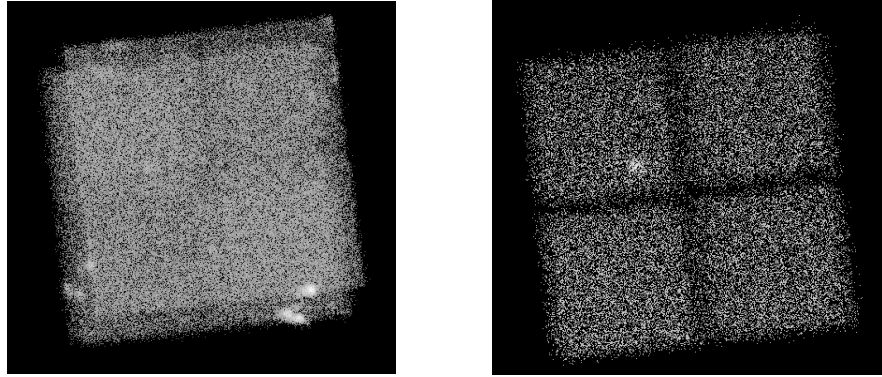


**Figure 1.13:** Left: sky image generated directly from level 1a data. Right: sky image generated from screened level 2 data. These two figures are produced from the same raw data. There are many criteria for data screening and the figure in the right is just an example.

### 1.6.1 Data Calibration

The first process is data calibration. In this step, two factors should be considered: the temporal change of mast and spacecraft's attitude. By using telescope's housekeeping files, the corrected data can be produced by *NuSTAR* software. There are some *NuSTAR* software modules for this process. Most of them are nearly automatically, which means once we have initial files, the output files are fixed. Therefore, we do not concentrate much on these software modules. Before we go into this module, some basic concepts should be introduced.

#### Grade of Data

When a photon interacts with a detector, the ideal condition is that only one pixel record this photon, which has better spectra resolution than other situations. But a single X-ray photon can be spread and received by more than one pixel. Generally, the less pixels by which a photon recorded, the better the event is. Naturally, there are different patterns of interaction between the photon and surrounding pixels. These patterns are listed in figure 1.14.

#### Status of Data

Just like flagging the quality of pixel data, it is necessary to flag event data because there are many factors that can trigger detectors. For instance, if we have a photon record in a detector, we need to know if it is from the source we are observing. Actually, cosmic rays can also trigger the detectors and we want to get rid of them in order to increase the signal to noise ratio. Therefore, after we have distinguished them from source photons, it is needed to be recorded for data screening—thus each single event has its status. In fact, similar to data's grade, status of data also has many patterns. For example, an event may fall into bad pixels, have a neighborhood bad pixel or fall into a hot pixel, etc. All these different situations are recorded by a 16-bit binary number and status of good event which is ideal for scientific analysis is all zero (recorded as "b0000000000000000").

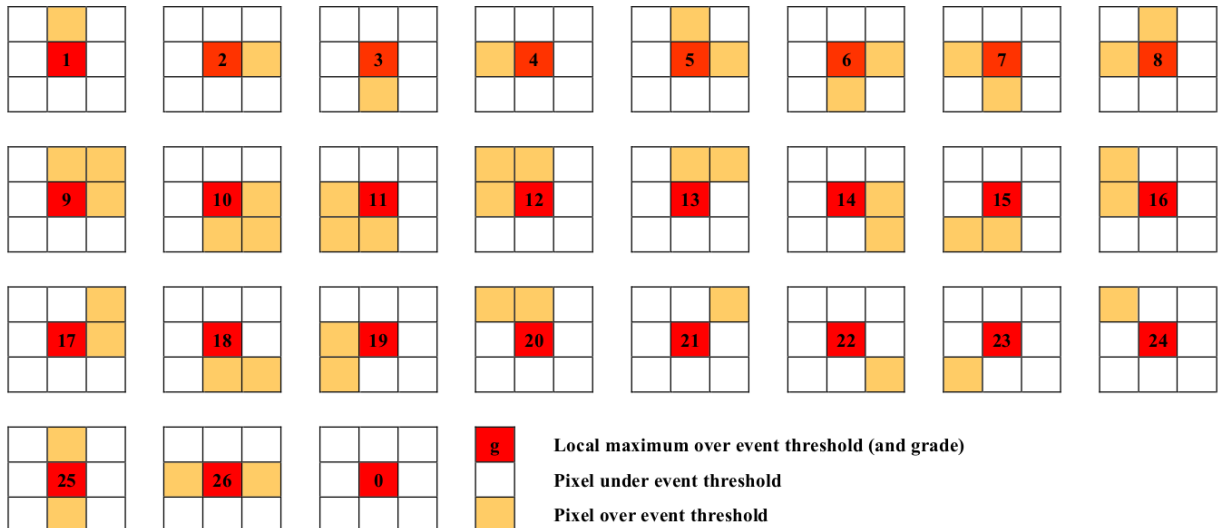


**Figure 1.14:** There are 33 different NuSTAR grades—from grade 0 to 32. In this figure, grades from 0 to 26 are listed because these grades are accepted by NuSTAR data screening by default. We can further get rid of some grades if needed.

### 1.6.2 Data Screening

After data calibration, though we know if one event is good or not, bad events are not excluded from original files. This is the primary reason of doing data screening. There are primarily 3 procedures in this step.

The first one is choosing good time intervals, which means remove some unwanted time intervals. For example, when the telescope is in the South Atlantic Anomaly, when the Earth is in the Field Of View and when the motion of mast is not well tracked, etc. Sometimes we need to add our own GTI (Good Time Interval) file to get better cleaned data. Then remove bad pixels and events flagged as bad in the last step (by using the information of data status). At last, choose the proper grade of data (the default value is 0-26).

The core module in this step is called 'nuscreen' and most of job is done by this software module. There are two parameters we mostly focus on—'gradeexpr' and 'statusexpr', which are used for choosing grade of data and status of data respectively. For example, gradeexpr=0-8 means choosing grade range from 0 to 8 and statusexpr="STATUS==b0000000000x0xx00 means leaving out bad events. We also can set them to default value by 'statusexpr=DEFAULT' and 'statusexpr=DEFAULT'. By adjusting these parameters' values, we can get a bunch of cleaned event files. Then we can generate several sky images and spectra and choose a better result.

### 1.6.3 Products Extraction

The aim of this process is to extract high-level scientific products including light curves, sky images, spectra, Ancillary Response Files (ARF) and Redistribution Matrix Files (RMF). ARF and RMF files are used for spectra analysis. The main software module is 'nuproducts' which generates these files automatically by passing some parameters. I mainly focus on two parameters which are 'pilow' and 'pihigh'. These two parameters filter

the energy range of cleaned stage 2 event files. The default values of the two parameters are 39 Pi and 1909 Pi respectively corresponding the *NuSTAR*'s energy range 3-78.4eV. But usually we choose pilow larger than 39 and pihigh smaller than 1909 in order to get more reliable data.

## *Chapter 2*

---

## Data Analysis

### 2.1 Data Analysis of Pulsar B1937+21 Using NuSTAR

Usually, we choose all the parameters to be default values. We may change some of the parameters in certain cases. Then we can produce a complete set of stage 2 files by using the module 'nupipeline'. The following is the sky images from *NuSTAR*'s module A and module B.

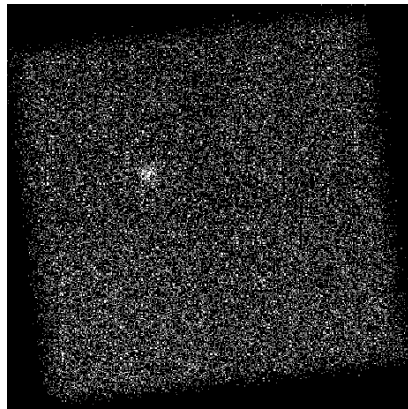


**Figure 2.1:** Sky image of module A

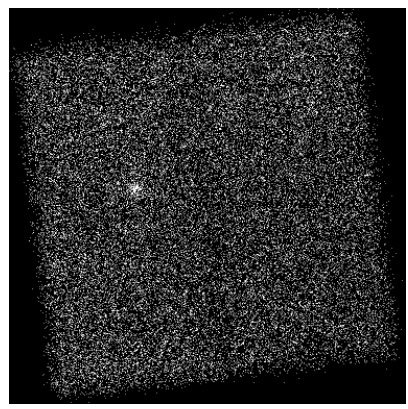


**Figure 2.2:** Sky image of module B

Although there are lots of background noises in these two pictures, the source is clearly identifiable. We can obviously see the differences between these two figures. For example, the source is sharper in the right figure. Actually, from figure 1.12 we can see that the PSF (half power diameter) of module B is slightly smaller than that of module A in each energy range. The focal plane module comprises 4 detectors, but in these figures we can barely distinguish different detectors. This implies that the data are not calibrated and screened well enough.

After getting cleaned stage 2 files, we can continue to generate light curves, spectra and so on. Before doing these, it is required to choose source and background regions. The figure 2.3 show the regions we choose.

In figure 2.3, the left green circle is source region while the right green circle is background region. The center of source circle is (19:39:38.561 ra, +21:34:59.126 dec) and

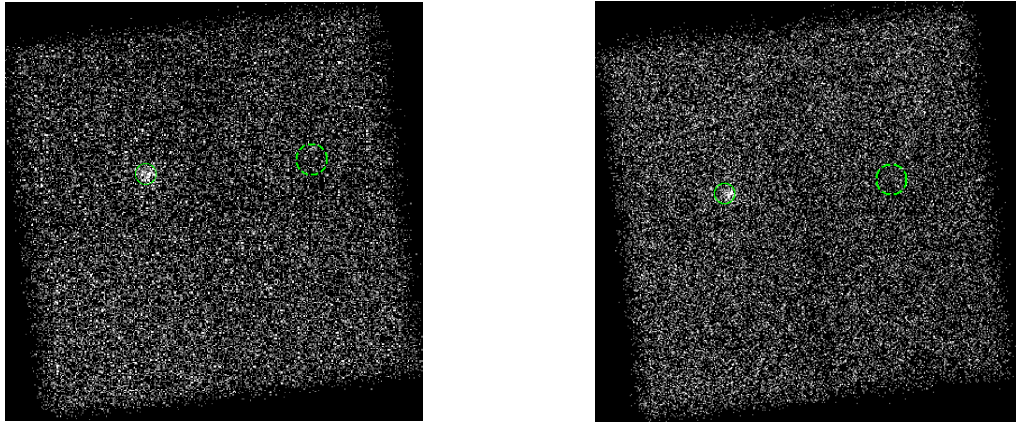


**Figure 2.3:** Source and background regions of module A (left) and B (right).

the radius is 23 arcseconds. The center of the background region is (19:39:12:412 ra, +21:35:29.210 dec) and the radius is 34.140 arcseconds. We call the choice of the source and background region as "region 1". The data of the source region center is from [ATNF](#) (Australia Telescope National Facility). From the figure 2.3 we can see that the source we observed is actually the right source—B1937+21. This means that the observation data can be used to analyse the pulsar B1937+21. However, for module B, the position observed source is a little bit away from the ATNF data. This means that we might need 2 sets of source and background regions for module A and module B respectively.

The figures 2.4 and 2.5 are the light curves of module A and B. These light curves are generated using ds9 software. The time interval of each bin is 50 seconds. The horizontal axis is time and the vertical axis is proportional to count rate. Although these pictures show periodicities, it does not mean that we can do timing analysis for B1937+21 by using *NuSTAR*. The reason is that the time resolution of *NuSTAR* is about 2 ms which is larger than the spin period of B1937+21 ( $\sim 1.56\text{ms}$ ). In fact, I think the periodicity reflect the *NuSTAR*'s orbital information to some extent. *NuSTAR*'s orbit is very low (the semi major axis is about 7000km) so its observation will be greatly influenced by the Earth. When the source is blocked by the Earth, the count rate is zero (after data calibration and screen)

The figure 2.6 is the spectra of module A and B. The group counts of both module A and B are 20 and the fitting model is multiplication of absorption of X-ray model (see in sherpa document '[xstbabs](#)') and 1 dimensional power law model (see also in sherpa document'[powlaw1d](#)'). We use chi square statistics to analyze goodness of fitting.

	Module A	Module B
Column Density (nH) ( $10^{22}\text{atoms}/\text{cm}^2$ )	4.06	0.012
Photon Index ( $\Gamma$ )	1.33	1.46
Reduced Chi Square Statistic	0.33	0.30

Table 2.1: Fitting result

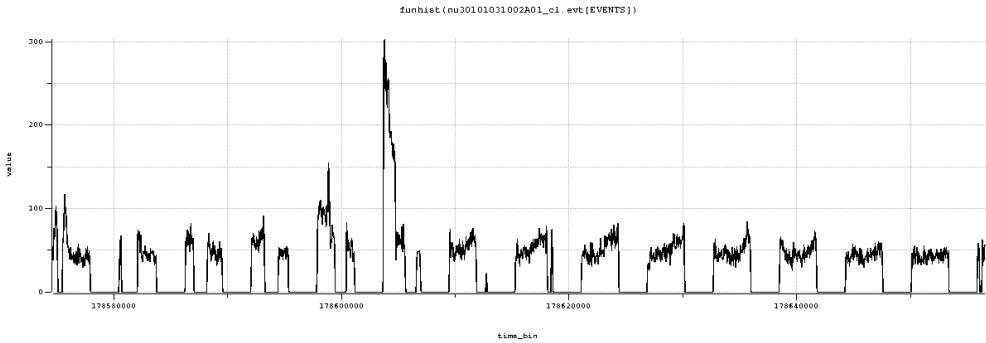


**Figure 2.4:** Light curve of module A

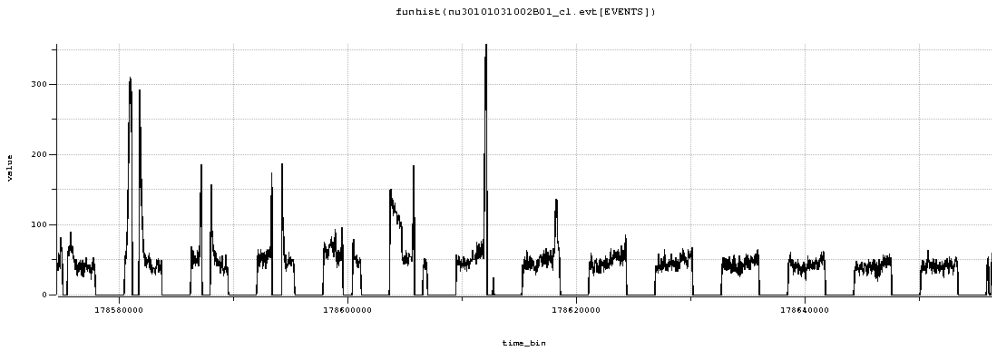


**Figure 2.5:** Light curve of module B

The table 2.1 lists some important parameters of the fitting result. The number of total points in spectrum of module A and B are both 11. For the spectrum of A, the reduced statistic is about 0.33 and Q-value is about 0.95. The fitted column density is about  $4.06 \times 10^{22} \text{ atoms/cm}^2$  and the photon index is 1.33. For the spectrum of B, the reduced statistic is 0.30 and Q-value is about 0.97. The column density is about 0.012 and photon index is 1.46. We observed that the column density difference between module A and B are huge (module A is about 400 times larger than module B). This is because that the high energy X-ray photons are nearly not absorbed by interstellar medium. As a result, the column density fitted only by *NuSTAR* ( $3\sim79\text{eV}$ ) reliable so we need to combine

*NuSTAR* data and *Chandra* and *XMM-Newton* data together to fit.

## Some Analysis

There are actually some problems in the whole process. First of all, the regions is not properly chosen. Although we can see that the pulsar is completely in the source region, it is not in the center of the source region (especially for module B). As for the background region, it is a little bit small. In addition, there are four detectors so it is better to choose the background and source region in the same detector.

Secondly, there are many spikes in light curves of both module A and B. Therefore we may need to clean the data more carefully. One straightforward way is to add our own GTI file rather than only using the default GTI file. Thirdly, the reduced statistic values for module A and B are 0.33 and 0.30 respectively, which are a little bit small. It means

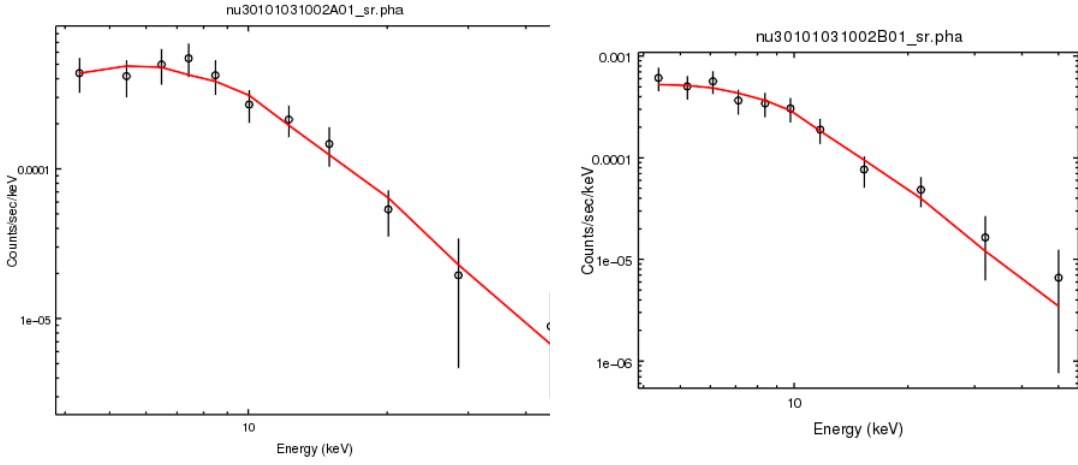


**Figure 2.6:** Spectra of module A (left) and B (right). The total source counts of A before grouping is 301 and B is 286. After subtracting background, the source counts of A is 193.45 and B is 170.25. Reduced chi square statistic: 0.33 (A) and 0.3 (B).

that our model is overfitted and the result seems to be too good to happen. In general, our model is good if reduced chi square statistic is about 1. Thus, we need to rethink how we should screen the data.

In short, we are focusing on the two things: change the source and background regions and filter the light curves by adding our own GTI file.

At first, we need to change the source and background regions. The figure 2.7 shows the region we choose this time. There are three major changes of the chosen regions. First of all, we slightly adjust the center of the source region in order to make the observed source be the center of the source region. The center is (19:39:38.101 ra, +24:34:56.838 dec). We do not change the radius of the source region so the radius is still 23 arcseconds. Secondly, we change the position of the background region and make it in the same region with the observed source. The center of the background region is (19:39:38.003 ra, +21:34:57.657 dec). The inner and outer radius (the background region is an annulus) are 40 arcseconds and 100 arcseconds respectively. The reason we choose the background region is that *NuSTAR* has 4 detectors and we want to get rid of the influence of instinct differences between the 4 detectors. Thirdly, we change the shape of background region from a circle to an annulus. Just as before, we call this choice of region as "region 2". The aim is to make the background region surround the observed source to be more like the background of the source.

At first glance, it seems that this time we choose the source and background region reasonably. But there are also some problems just as the following figure 2.8 showing. The *NuSTAR* is composed of 4 separate detectors that work independently with each other. Therefore, we should make sure that the background region we choose does not cross the border of one detector. Thus, we change the background region to the "region 3" as the right part of the following figures show (figure 2.8) and keep on using the "region 3" in the following discussion of this section. Meanwhile, because we want to try to do timing analysis, barycenter correction is also applied in the following analysis. So far, we have changed 2 things: background region and barycenter correction.

The figures 2.9 and 2.10 are the light curves of the module A and B respectively

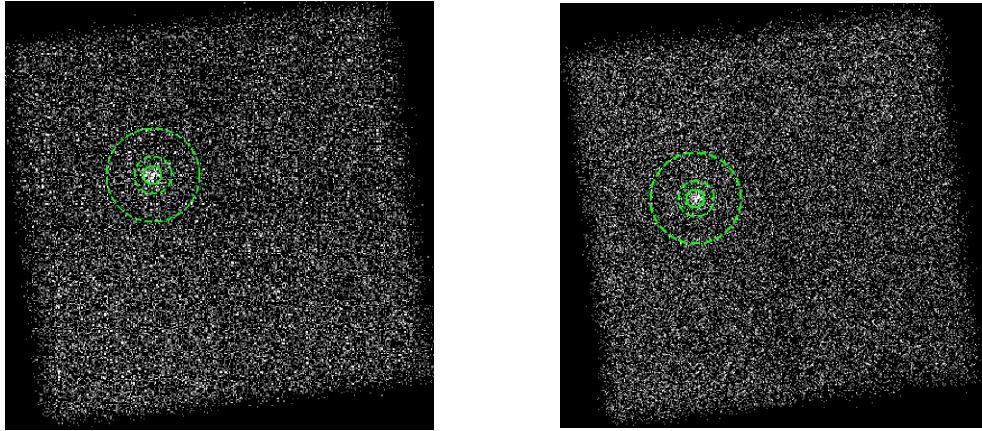


**Figure 2.7:** Source and background regions of module A (left) and module B (right).

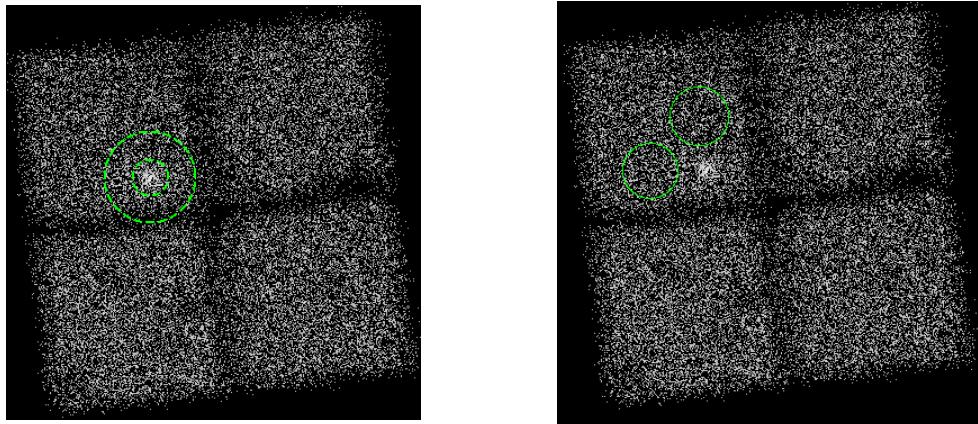


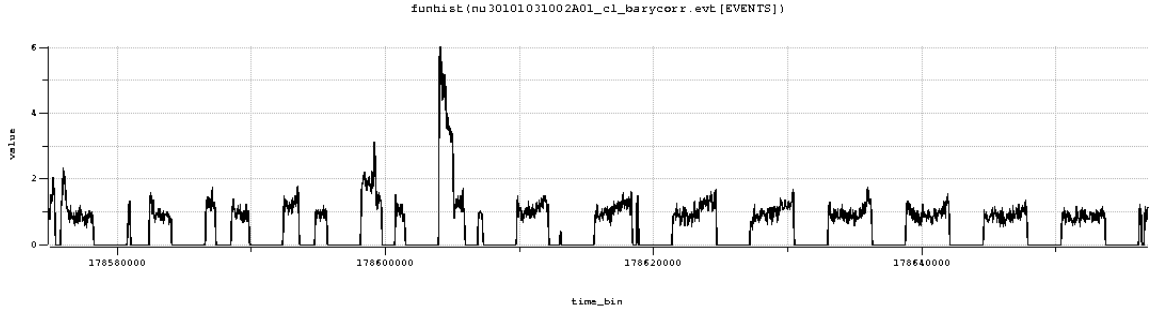
**Figure 2.8:** The problems of the annulus background region (denote as "region 2", left) and the background region we choose again (denote as "region 3", right).

after changing the source and background regions. The bin time is also 50 seconds. The horizontal axis represents time and the vertical axis represents count rates. Actually there is no obvious improvement in light curves after we change the source and background regions — there are also some spikes in the light curves. In order to get rid of those high spikes, we add some GTI files to filter the event file.

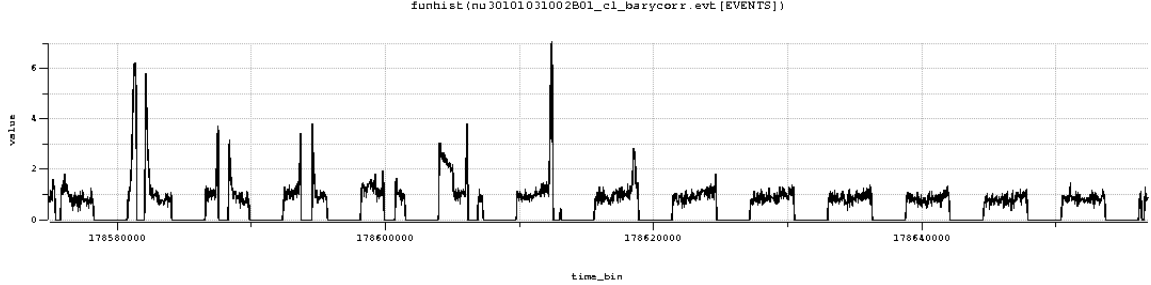
	Module A	Module B
Column Density (nH) ( $10^{22} atoms/cm^2$ )	$6.46 \times 10^{-6}$	$1.75 \times 10^{-5}$
Photon Index ( $\Gamma$ )	1.10	1.53
Reduced Chi Square Statistic	0.74	0.53

Table 2.2: *Fitting result*

The figure 2.11 is the spectra of module A and B. The table 2.2 show some key parameters of fitting result. The fit model and method are the same as before. For module A, the reduced chi square statistic value is about 0.73 and Q-value is 0.65. For module B, the reduced chi square statistic is about 0.51 and Q-value is 0.83. After changing the source and background regions, the reduced chi square statistic values of both module A and B are greatly increased while the Q-values are largely decreased. This means that the observation data is less overfitted by our model, which generally is a better result.



**Figure 2.9:** Light curve of module A



**Figure 2.10:** Light curve of module B

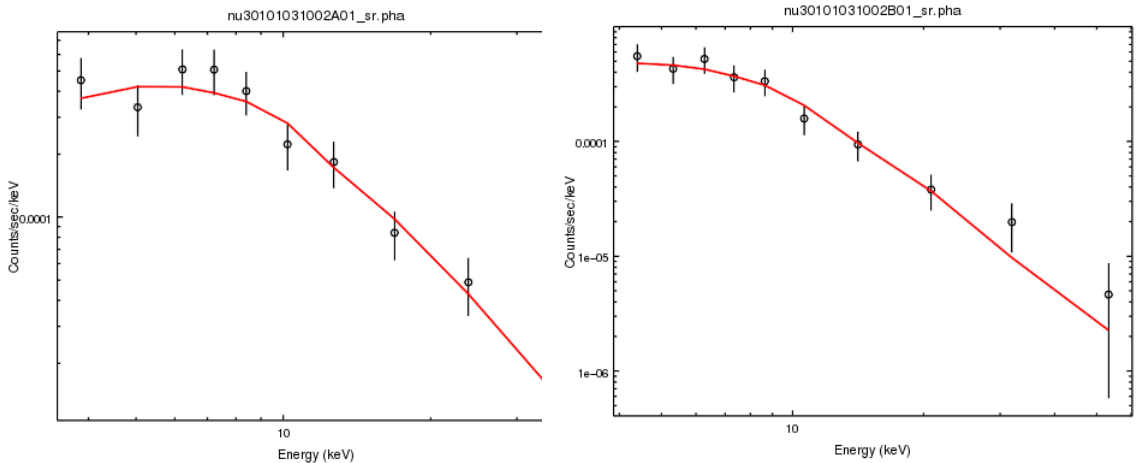


**Figure 2.11:** Spectra of module A (left) and B (right). The total source counts of A before grouping is 264 and B is 254. After subtracting the background counts, the source counts are 188.23 (A) and 161.97 (B). Reduced chi square statistic: 0.74 (A) and 0.53 (B).

Now we consider using our own GTI file to filter the light curves we get before in order to get rid of spikes. We use **"dmextract"** and **"deflare"** tools to extract GTI files. The figures 2.12 and 2.13 are the light curves after filtering event files by our own GTI files.

The above light curves look much better than the previous light curves (figure 2.12 and figure 2.13). All extremely high spikes are removed. We also have applied barycenter correction in this step. After adding the GTI file, the cleaned event files are changed too. As a result, the spectra should also have some changes. The figures 2.14 are spectra produced by using GTI files we generated.

The table 2.3 shows some critical parameters of the fitting result. We can see that adding our own defined GTI file will apparently affect the result of spectra fitting. The photon index change from 1.10 to 1.20 for module A while the photon index change from

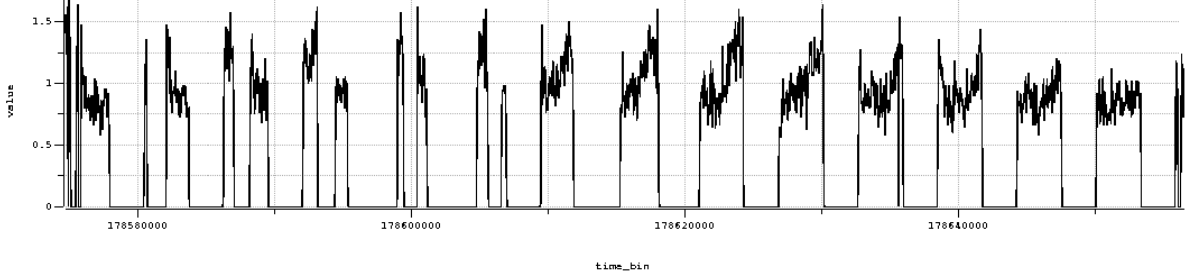


**Figure 2.12:** Light curve of module A after adding our own GTI file

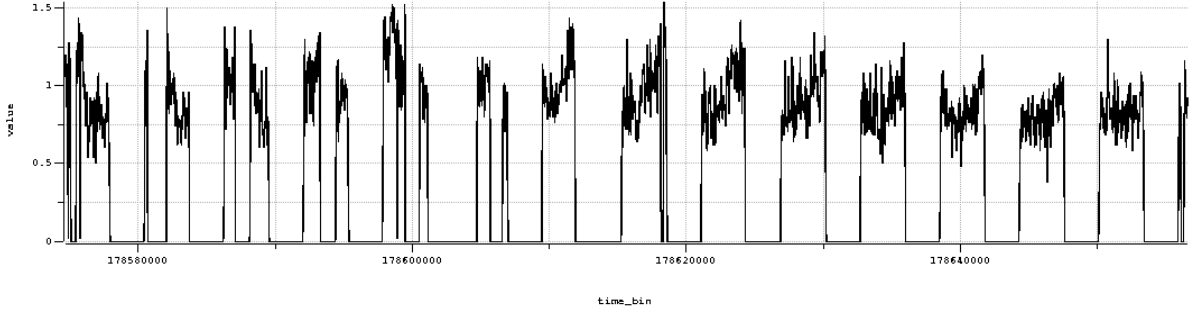


**Figure 2.13:** Light curve of module B after adding our own GTI file

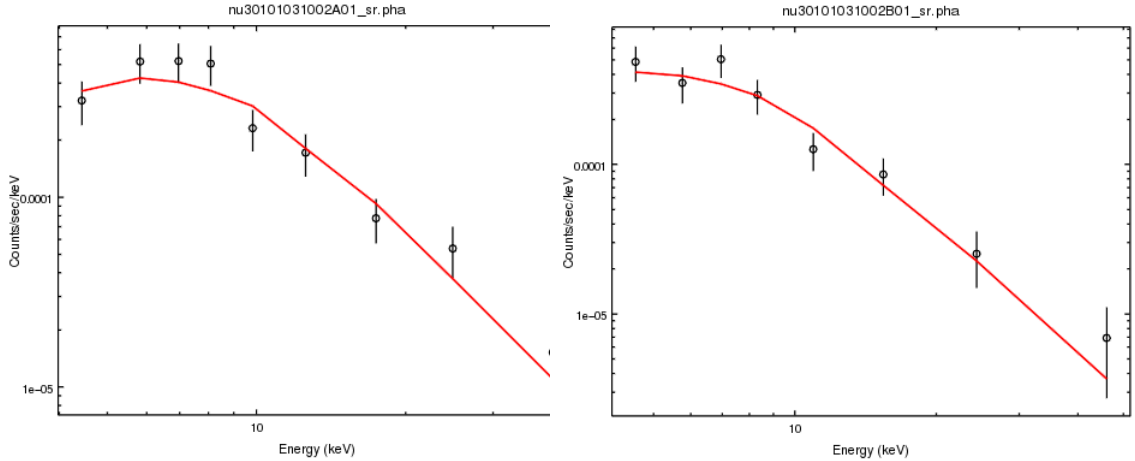


**Figure 2.14:** Spectra of module A (left) and B (right) after adding our own GTI files. The total source counts of A before subtracting background is 238 and B is 211. After subtracting background counts, the source counts of A is 177.78 and B is 139.46. Reduced chi square statistic: 1.13 (A) and 0.98 (B).

1.53 to 1.48. Besides, the chi square statistic changes dramatically for both module A and B (nearly doubled). We notice that the column density for module A and B differs greatly. I think we can ignore this for now because hard X-ray is nearly not affected by interstellar medium. We will care about column density after combined with other telescopes data such as Chandra.

Then, we want to combine the module A and B data to fit the spectra together. This leads to a question. We know that there are some intrinsic differences between module A and B of *NuSTAR*. As a result, how do we combine two modules together to generate one spectrum? There are two ways of doing this. Firstly, we can directly fit the spectra of these two modules with one single model. Secondly, we can add a constant between module A and B to represent the differences.

	Module A	Module B
Column Density (nH) ( $10^{22} atoms/cm^2$ )	7.57	$4.65 \times 10^{-8}$
Photon Index( $\Gamma$ )	1.20	1.48
Reduced Chi Square Statistic	1.13	0.98

Table 2.3: *Fitting result with user defined GTI files*

## *Chapter 3*

---

### **Gamma-Ray Analysis**

As mentioned before, because of the very short rotation periods, MSPs have very small light cylinder radii compared with normal pulsars. As a result, their emission mechanisms are similar to normal pulsars, especially for my target objects — PSRJ0218+4232, PSRJ1939+2134 and PSRJ1824-2452 which are among the fastest spinning MSPs. Therefore, as normal pulsars, these three pulsars are bright in Gamma-Ray band so it is convenient for us to analyze the spectra properties of them in gamma-rays.

### **3.1 Gamma-Ray Emission Mechanism of MSPs**

An MSP's magnetosphere is dominated by various kinds of emission mechanisms. Thus we should review some fundamental emission mechanism firstly, including synchrotron radiation, curvature radiation and inverse-Compton radiation.

#### **3.1.1 synchrotron radiation**

Synchrotron radiation is a special case of cyclotron radiation when particles' speed is comparable to the speed of light. Because of the relativistic beaming effect, we will observe a very short radiation pulse when speed of particles is large. We only aim to analyze the spectrum properties of MSPs, so we focus on the spectrum property of synchrotron radiation. The power spectrum of a single electron can be described by the function 3.1

$$P(\nu) = \frac{\sqrt{3}e^3 B \sin \alpha}{mc^2} \left( \frac{\nu}{\nu_c} \right) \int_{\nu/\nu_c}^{\infty} K_{5/3}(\eta) d\eta \quad (3.1)$$

where  $\nu_c$  is the critical frequency and  $K_{5/3}$  is modified Bessel function. The critical frequency can be expressed by the function 3.2

$$\nu_c = \frac{3}{2}\gamma^2 \nu_{cyc} \sin \alpha \quad (3.2)$$

where  $\alpha$  is the pitch angle and the  $\nu_{cyc}$  is the frequency of corresponding cyclotron radiation.

These function does not give us very much information because of the integration of the modified Bessel function. We let  $x = \nu/\nu_c$  and fix the environment variables such as magnetic field ( $B$ ), the function 3.1 becomes:

$$P(\nu) = C \times x \int_x^\infty K_{5/3}(\eta) d\eta \quad (3.3)$$

where  $C$  is a constant dependent on  $B$ . Thus, in order to analyze the power spectrum of synchrotron radiation, we only concentrate on the later part, which is

$$F(x) = x \int_x^\infty K_{5/3}(\eta) d\eta \quad (3.4)$$

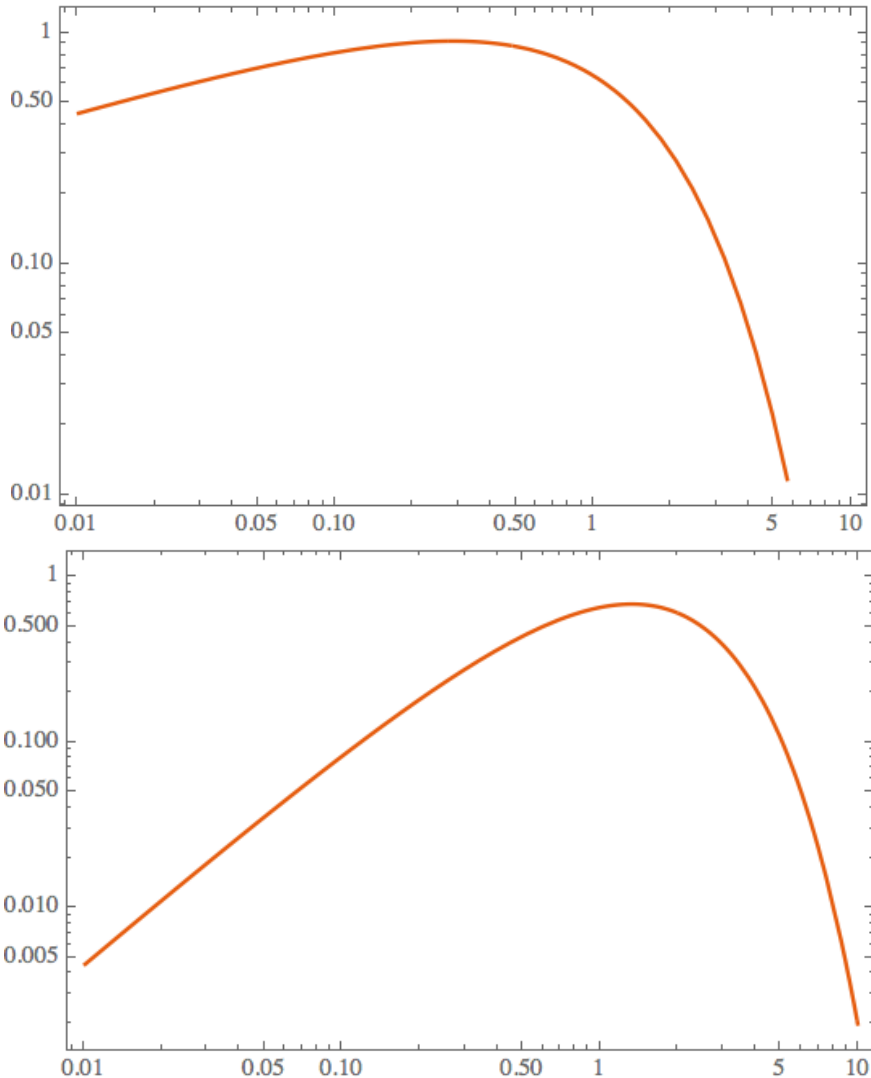


**Figure 3.1:** According to the function 3.4, top:  $F(x)$ ; bottom:  $xF(x)$ .  
<change>should change the style of the figure.</change>

The top figure 3.4 describes the general shape of power spectrum of synchrotron radiation. When the frequency is larger than the critical frequency  $\nu_c$ , the power goes down dramatically. However, the top figure does not show the information that at what frequency the electron emit the strongest power, which is in the bottom figure. The bottom figure shows that the energy most energy emitted around critical frequency.

In reality, synchrotron radiations are not generated by a single particle. We describe the number density distribution of electrons with respect to energy by a single power-law model as the function 3.5 shown.

$$N(E) \approx CE^{-\delta} \quad (3.5)$$

For simplicity, we set the ambient magnetic field  $B$  to be a constant and make an approximation that all radiations are at a single frequency:

$$\nu \approx \gamma^2 \nu_{cyc} \quad (3.6)$$

where the meaning of  $\nu_{cyc}$  is the same as function 3.2. Our objective is to know the relationship between total power of all electrons and their radiation frequency. We describe the relationship as the function 3.7

$$-P(E)N(E)dE = Q_\nu d\nu \quad (3.7)$$

$$P(E) = \frac{4}{3}\sigma_T \beta^2 \gamma^2 c U_B \quad (3.8)$$

where  $\sigma_T$  is electron Thompson scattering section,  $U_B$  is energy density of the environment magnetic field,  $Q_{nu}$  is the emission coefficient of synchrotron radiation and  $E = \gamma m_e c^2$ . With function 3.6, we have

$$P = \frac{dE}{d\nu} = \frac{m_e c^2}{2\sqrt{\nu \nu_{cyc}}} \quad (3.9)$$

Combine the function 3.9 and 3.7 we get:

$$Q_\nu = \frac{4}{3}\sigma_T \beta^2 \gamma^2 c U_B \frac{m_e c^2}{2\sqrt{\nu \nu_{cyc}}} N(E) \quad (3.10)$$

By ignoring constants in the function 3.7 we have

$$Q_\nu \propto \nu^{(1-\delta)/2} \quad (3.11)$$

The function 3.11 shows that if the number density electrons is a power-law distribution, the spectrum of synchrotron radiation is also a power-law model.

### 3.1.2 Curvature Radiation

When particles move along the curved magnetic field lines, they will generate curvature radiation. This is exactly the case in a pulsar's magnetosphere. The magnetic field is so strong that relativistic charged particles (electrons and positrons) are forced to move along the magnetic field line and hence emit strong curvature radiation.

<add>continue from here</add>

### 3.1.3 Inverse-Compton radiation

<add>inverse-compton radiation</add>

### 3.1.4 Two-layer Model

After we have reviewed gamma-ray fundamental emission mechanism, we can proceed to the Two-layer model on which this thesis is mainly based. Two-layer model is a variation of outer-gap model since they both claim that the gamma-ray emission zone is close to the light-cylinder. However, in two-layer model, the outer layer consists of two regions — a primary acceleration region and a screening region.

In the primary region, charged particles moved out of pulsars along the open field lines, so the charge density is usually very low. However, by pair-production processes, a lot of  $e^-$  and  $e^+$  are produced. But in the primary region where lots of pairs are created, the charge density doesn't change very much because the pairs have not been separated yet. With the help of strong electric field, the particles of different signs move to opposite directions. As a result, the two-layer model states that just above the primary region, a screening region will be created and the charge density is very large. This is basically the reason why there are two regions in pulsars' outer magnetosphere.

Then the next issue is that how we describe the distribution of charge density in these two regions. For simplicity, we just use a step function to represent the charge density distribution and step function can clearly shows the gap between the two regions. We use a magnetic dipole model to approximate the magnetic distribution in the magnetosphere. Since in magnetic dipole model, magnetic field at one position is only dependent on the position's distance from the source and altitude, we can also ignore the azimuthal distribution of charge density in our model and use the two parameters the  $r$ (distance) and  $\theta$ (altitude) to calculate the magnetic field at some position.

In the two-layer model, we can use three parameters to express the structure of a pulsar's outer magnetosphere - charge density of the primary region, the total length of the primary region and the screening region and the last one is the ratio of the thickness of the primary region and the screening region. The figure 3.2 shows the basic structure of two-layer model.

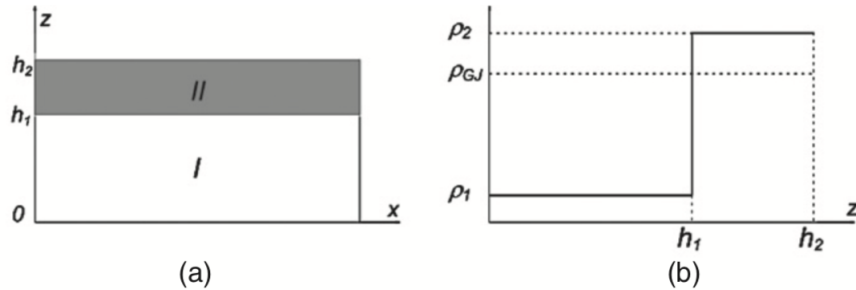


**Figure 3.2:** (a): The geometry of two-layer model.  $h_1$  and  $h_2$  is the height of the primary region and the screening region respectively. (b): the charge densities of primary region and screening region. In the primary region, the charge density is much smaller than Goldreich-Julian charge density while is larger in the screening region. *<mayChange>this figure is from the previous paper, I may need to regenerate the figure.</mayChange>*

As the figure 3.2 showing, let the charge density of the primary region be  $\rho_1 = (1 - g_1)\rho_{GJ}$  and the total gap size is  $h_2$ , where  $\rho_{GJ}$  is Goldreich-Julian charge density. For convenience, we also denote the gap size of the primary region as  $h_1$ .

We denote the electrical potential to be  $\phi_0$  which satisfies

$$\nabla^2 \phi_0 = -4\pi \rho_{GJ} \quad (3.12)$$

and the total electrical potential is  $\phi = \phi_0 + \phi'$ , where  $\phi'$  is a representation of the deviation of the co-rotating electrical potential. Let total charge density is  $\rho$  and subtract the equation 3.12 we have

$$\nabla^2 \phi' = -4\pi (\rho - \rho_{GJ}) \quad (3.13)$$

Because the model has ignored the distribution in the azimuthal direction, we can use two parameters  $x, z$  to represent a position, where  $x$  is the direction along the magnetic field line and  $z$  is the perpendicular to the magnetic field line. In order to solve the equation 3.13, the model also makes 2 approximations. The first is that the directive of electrical potential  $\phi$  is ignored. The second is that the Goldreich-Julian charge density is uniformly distributed along the magnetic line direction ( $x$  direction). These 2 approximations are based on the a reasonable assumption that the change rate for both electrical potential ( $\phi'$ ) and Goldreich-Julian charge density ( $\rho_{GJ}$ ) along the  $x$  direction is much smaller compared with  $z$  direction. As a result, the equation 3.13 can be written as:

$$\frac{\partial^2}{\partial z^2} \phi' = -4\pi (\rho - \rho_{GJ}) \quad (3.14)$$

In order to solve the equation 3.14, we have to have proper boundary conditions. First of all, we have to decide the boundary positions, which is determined by 4 parameters and they are  $x_{lo}, x_{hi}, z_{lo}, z_{hi}$ . It is reasonable to set  $x_{lo}$  and  $x_{hi}$  be the pulsar's surface and the light cylinder respectively and  $z_{lo}$  (lower boundary) be the last open field line. And let the electrical potential be 0 along the last open field line (this is because we have ignored the variation of electric field in  $x$  direction).

$$\phi(x, z_{lo}) = 0 \quad (3.15)$$

The position of  $z_{hi}$  is a little bit tricky. In order to make the electrical potential be continuous at  $z = z_{hi} = h_2$ , the model sets the  $\phi' = 0$  since the non-corotating electrical potential outside the upper bound is 0 and the co-rotating potential is continuous near the boundary.

With these boundary conditions and equation 3.14, we can calculate the distribution of electric field, which accelerates charged particles to a very high speed so that they can emit curvature radiation, giving gamma-ray spectra. With the accelerating electric field known, we can calculate the Lorentz factor of charged particles and their spectra. This is the basic idea of the Two-layer model. <question>not sure if I should introduce the theory more thoroughly</question> .

<question>I am not sure if I should add this part here, since it is completely based on my own experience</question>

### **Constraints of The Two-layer Model Used In The Thesis**

The simplified two-layer model is consistent with observation data to some extent. (The relevant data can be found in the paper *GAMMA-RAY SPECTRAL PROPERTIES OF*

*MATURE PULSARS: A TWO-LAYER MODEL)* The model uses 4 parameters to get a fair good prediction of gamma-ray spectra for many pulsars. And all these 4 parameters have a very obvious physical meaning. However, we can clearly find the "defects" of the model — it is somewhat oversimplified. Though there are other more sophisticated version of two-layer model, we use the simpler one, which may cause some inconsistency between our simulation and observation.

Therefore, we can briefly analyze which part is oversimplified and can be improved. First of all, we directly use a step function to describe the charged particle distribution. Though the charge density of the screening region is much larger than the primary region, using a step function is non-physical and may exaggerate the change rate of charge density.

<add>continue from here</add>

## 3.2 Introduction of The Fermi Gamma-ray Space Telescope

The Fermi Gamma-ray Space Telescope was launched on June 11, 2008 and opened a new window of studying supermassive black-hole systems, pulsars and so on. Its original name was Gamma-ray Large Area Space Telescope (GLAST) and changed to Fermi Gamma-ray Space Telescope in honor of a great scientist Enrico Fermi.

The Fermi Gamma-ray Space Telescope contains two parts: Gamma-ray Burst Monitor (GBM) and Large Area Telescope (LAT), which is the primary components and is at least 30 times more sensitive than all gamma-ray telescopes launched before. We only use LAT for our purposes. So we focus on the LAT instrument, which contains four main subcomponents including tracker, calorimeter, anti-coincidence detector and data acquisition system. The reason why the telescope is designed in this way is that high-energy gamma-rays cannot be refracted by lens or mirrors. As a result, the way that the Fermi LAT operates is totally different.

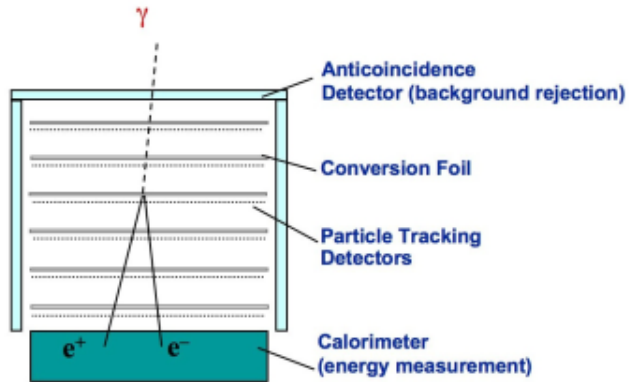


**Figure 3.3:** Light curve of module A

The following figure 3.3 demonstrates the very basic idea of the Fermi LAT working principles.

- Gamma-ray photons can enter the anti-coincidence detector freely while cosmic-rays will generate signals which can tell the data acquisition system to reject these

particles. In this way, the Fermi LAT can distinguish the gamma-ray photons and high energy cosmic rays and the confidence is over 99.9%.

- The conversion foil (shown in the figure 3.3) can convert the gamma-ray photons into electron and positron pairs. This procedure makes it possible to determine the directions of the coming gamma-ray photons.
- The tracker (particle tracking detectors in the figure 3.3) records the positions of the electrons and positrons generated from the gamma-ray photons. There are many trackers so the paths of a particle can be constructed.
- The electrons and positrons reach the calorimeter hence their energies are also measured. Therefore, the energies of the original gamma-ray photons can also be calculated.
- The data acquisition system rejects unwanted particles such as cosmic rays by the method we mentioned before. Also, photons come from the Earth's astronomers are also rejected.

For a telescope, the ability of measuring the light direction and energy is very crucial. From the above descriptions of the Fermi LAT working principles, we know that the preciseness of construction of particles' path heavily influences how good we can measure the direction of photons. And this process is greatly dependent on algorithms, which means that with the improvements of software, the sensitivity of the telescope can also be improved. The Pass 8 data was released on June 24, 2015. It is an reprocessing of the entire Fermi mission dataset with better energy measurements, larger effective area, wider energy range and so on. This is part of the reason why I will redo the analysis of the three MSPs.

### 3.3 Analysis With Fermi LAT

In this section, my main objective is to show the results of my analysis. Before doing so, it is appropriate to briefly introduce some terminologies.

- The first is count maps. A count map is basically generated by the following steps. Firstly we choose a pixel with a certain size. Then we check each photon's direction to determine if the photon is in this pixel. If it is in the pixel, the photon counts of the pixel will add one. So more photons fall within the pixel, the more photon counts the pixel has, hence the brighter the pixel is. By doing the same thing for every pixel, a count map is generated. A count map let us know what we have observed intuitively and gives us a very basic idea of if we get the wanted data.
- A count cube is very similar to a count map, except that a count cube is divided in many energy bands. For example, a dataset whose energy is from 100MeV to 100GeV can be divided into 30 bins. We can generate a count map in each energy bin, so we have 30 count maps. In other words, we can regard a count cube as multiple count maps.

- TS value provides us a way to test if our target source is observed. The TS value is:  $TS = -2\frac{\ln L_{max,0}}{\ln L_{max,1}}$ , where  $\ln L_{max,0}$  is the maximum likelihood value without the target source while  $\ln L_{max,1}$  is the maximum likelihood value with the target source. According to the equation, the smaller the ratio of  $\ln L_{max,0}$  and  $\ln L_{max,1}$ , the larger the TS value is. Therefore, a larger TS value statistically means that our aimed source is observed.
- <**add**>may have more items</**add**>

The basic idea of fitting spectra parameters is to make the count cube generated by the model be as similar to the observation data as possible. The calculation process can be summarized as follows. First of all, we have to generate a spectral model for every source in the region of interest based on the Fermi database. The database includes LAT four-year Point Source Catalog (3FGL), Galactic diffuse emission (gll\_iem\_v06.fits) and isotropic emission (iso\_P8R2\_SOURCE\_V6\_v06.txt). Then we can produce a count cube based on the model. Generally speaking, the difference of the count cubes between the model and observation is obvious. Then, the Fermi software adjusts the parameters to make the difference smaller. Until the errors are acceptable, the software outputs the final fitted parameters.

We use a power-law-exponential-cutoff (PLExpCutoff) model to fit the observation data and it is a special case of power-law-super-exponential-cutoff (PLSuperExpCutoff) model. The spectrum of PLSuperExpCutoff can be described by the function:

$$\frac{dN}{dE} = N_0 \left( \frac{E}{E_0} \right)^{\gamma_1} \exp \left( - \left( \frac{E}{E_c} \right)^{\gamma_2} \right) \quad (3.16)$$

where  $N_0$  is prefactor,  $E_c$  is the cutoff energy and the  $E_0$  is just a scale. PLExpCutoff model is the special case when  $\gamma_2 = 1$ . Our aim is to fit the parameters  $N_0$ ,  $E_c$  and  $\gamma_1$  to make the model be more consistent with observation data.

### 3.3.1 PSR J0218+4232

Our ROI is a circle with radius of  $20^\circ$  and all parameters of sources which are  $8^\circ$  outside of the center are fixed. For sources within  $8^\circ$ , their parameters are same as the default values. In our case, there are 7 point sources which have free parameters. In the figure 3.4, the green circles represent those free sources while the purple circles represent fixed sources. We need to notice that in the outer parts of the count map, there are some of very bright sources which have no free parameters. The reasons is that the they are so far away from our target source that the Fermi telescope can distinguish if a photon comes from the target source or the outer source. However, it is another case for the nearby sources.

#### Count Maps And Count Cubes

In the left of the figure 3.4 is the count map of PSR J0218+4232. In the center of the left figure, we can clearly see our target source. The dimension of the figures seems to be weird and the reason why we have 141 pixels for both x and y axis is that we select a

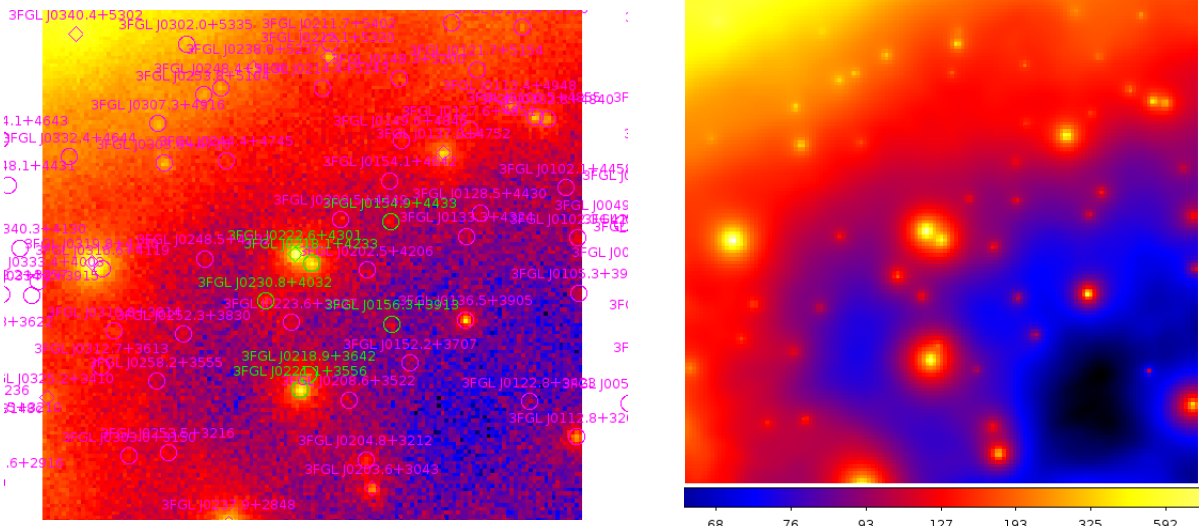


**Figure 3.4:** The count map of PSR J0218 (left) and the count map generated by the model. In the left figure, the green circles are free sources while the purple circles are fixed sources. The size of the figure is 141 pixels  $\times$  141 pixels, and each pixel is  $0.2^\circ \times 0.2^\circ$ .

<change>The figure color bar is a problem. I need to use some other tools to merge the two color bars.)</change>

circle region from the original data. However, when we generate a count map, we have to assign the sizes for x and y axis separately, which means that our a count map is actually rectangular. As a result, we have to crop a rectangular from the original circle region and in this case, we choose the rectangular as a square.

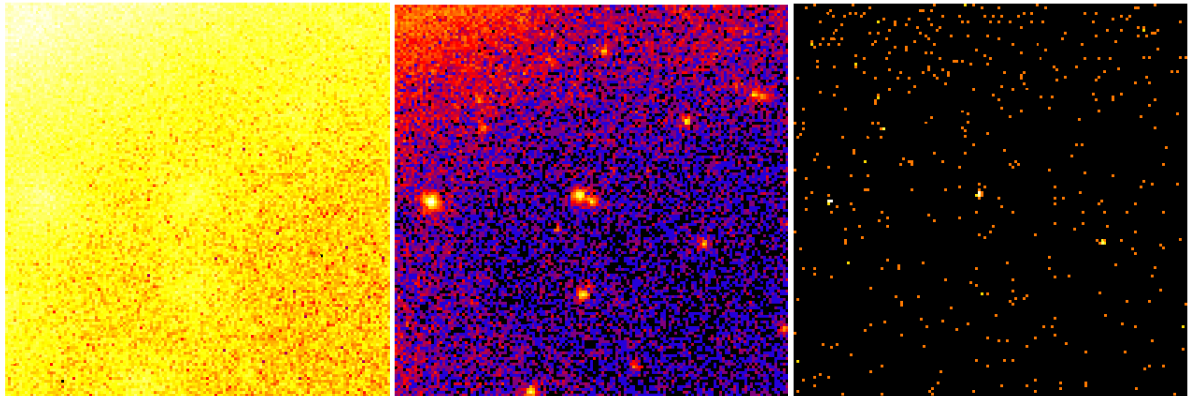


**Figure 3.5:** Three figures of PSR J0218+4232's count cube. The energy range of the figure in the left: 100~123MeV, middle: 1.873~2.310GeV, right: 35.11~43.29GeV.  
<add>add color bar</add>

The figure 3.5 is a comparison of PSR J0218+4232's count maps in different energy bands. The count map in about 100MeV is so messy that we can hardly distinguish our target source while in about 30GeV so faint that there are no recorded photon around the source. We choose three circle regions whose center are the our target source and the radii are 1000 " for all of the three figures and calculate the total photon counts of the selected regions. As the following table 3.1 shown, though total photon counts around our target source are similar between the left and middle map, the counts per energy is quite different. Therefore, we focus more on the middle energy parts (500MeV  $\sim$  50GeV). This means that when doing binned analysis, we divide more bins in the middle part.

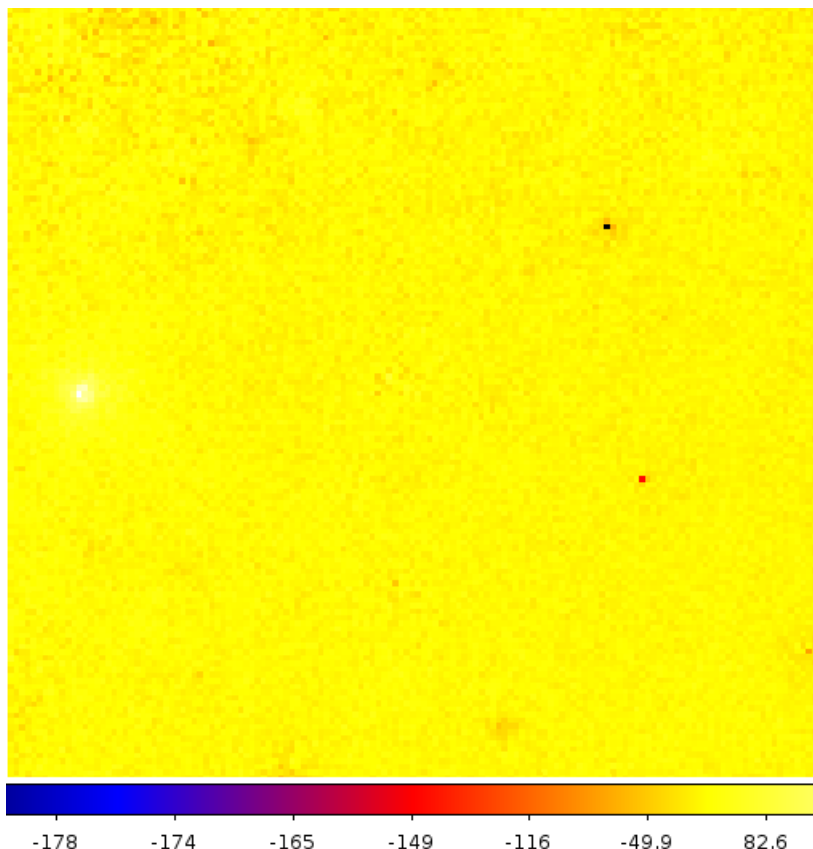
	Left	Middle	Right
Total counts	78	93	0
Energy range (MeV)	100~123	1873~2310	35110~43290
Counts / MeV	3.39	0.213	0.000

Table 3.1: *Photon counts of count maps in different energy bands.*

### Binned Likelihood Analysis

The figure 3.4 shows that the fit result of the model is similar to the observation. However, there are lots of small red pixels in the left figure (generated directly by the observation data) while the right figure is very "clean". This means that a lot of photon are thought as generated by the modeled source so in our model, the sources are generally slightly brighter than the observation. However, our target source is an exception. In the region we have used before (the center is the target source, and the radius is 1000''), the total photon count in the left figure is 1815 compare to 1737 in the right figure.

The reason why the count map generated directly by the observation data is a lot more messy is that our modeled source is generated according to the Fermi database and their spatial position is fixed. This means that if a photon comes from a particular direction and there is no any known pulsar in this direction, this photon has to be modeled to other direction. Thus, the spatial position of the photon is different between the observation and the model.



**Figure 3.6:** The residual map shows the difference between the observation and the model. It is generated by subtracting the photon counts of each pixel between the count maps of observation and the model. <**change**>ugly, scale may be wrong</**change**>

The figure 3.6 generally describes how well our model is compared to the observation data. There are some black dots and bright dots in the residual map which means that the absolute photon counts between the model and the observation differ a lot. However, it is acceptable because the original value is much larger. The absolute values of most of other pixels are less than 10 implying that the global fit is fine.

	Value	Error
Prefactor ( $N_0$ )	$1.71 \times 10^{-11}$	$0.0610 \times 10^{-12}$
Index1 ( $\gamma_1$ )	1.8999	0.0395
Cutoff ( $E_c$ , MeV)	3794.25	396.447

Table 3.2: Fit parameters of the model. The parameters are corresponding to the equation 3.16.  
<add>add comparison with previous data later.)</add> <change>the table is ugly</change>

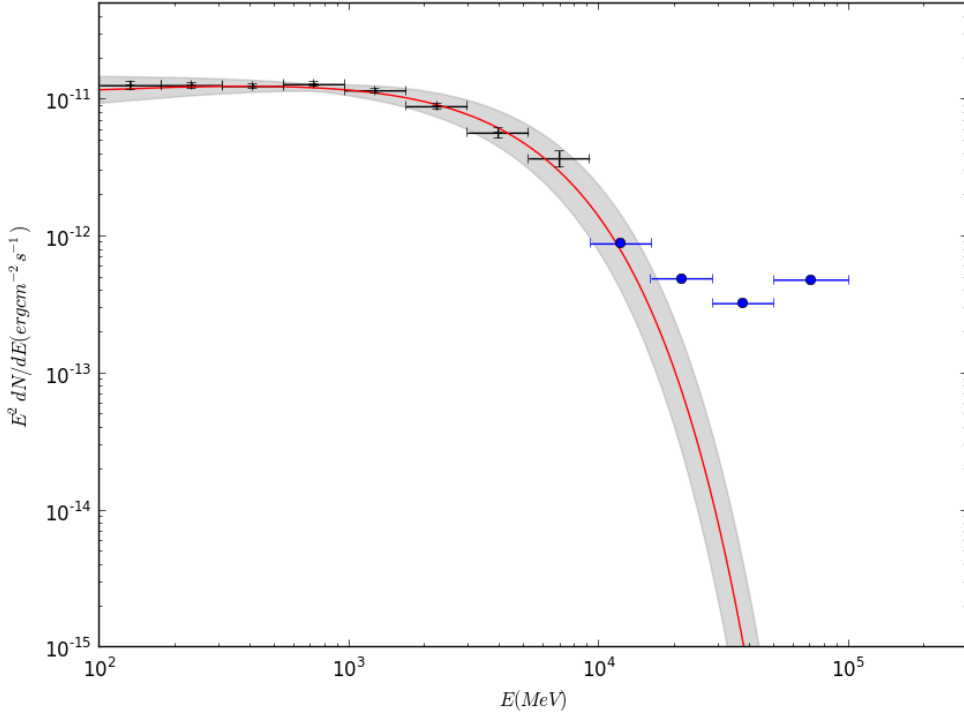


**Figure 3.7:** The log-log plot of flux to energy. The grey shade represents fitting errors, black points with error bars are flux points, the blue dots are upper values and the red line is the PLExpCutoff model multiplied by  $E^2$ . Flux points are fitted separately by dividing the total energy bin ( $100 \text{ MeV} \sim 100 \text{ GeV}$ ) into multiple energy bins. The horizontal error bars represents the width of each bin.

(The figure should use legends, but for now I have problem setting those styles, may be my matplotlib version is too old.)

<change>legends, arrows</change>

The table 3.2 lists the results of fitting parameters. The figure 3.7 plot the spectrum according to the function 3.16. One thing should be noticed is that we need to multiply  $E^2$  to the function 3.16 to get the flux. The figure 3.7 shows that the global fit is consistent with flux points fitted by each energy bin separately. The TS value for the fit is 7110, which gives us a significance level  $\sigma \approx \sqrt{TS} = 84$ . This strongly implies the presence of our target source. We can also use a TS map to test the presence of the source as the figure 3.13 showing.

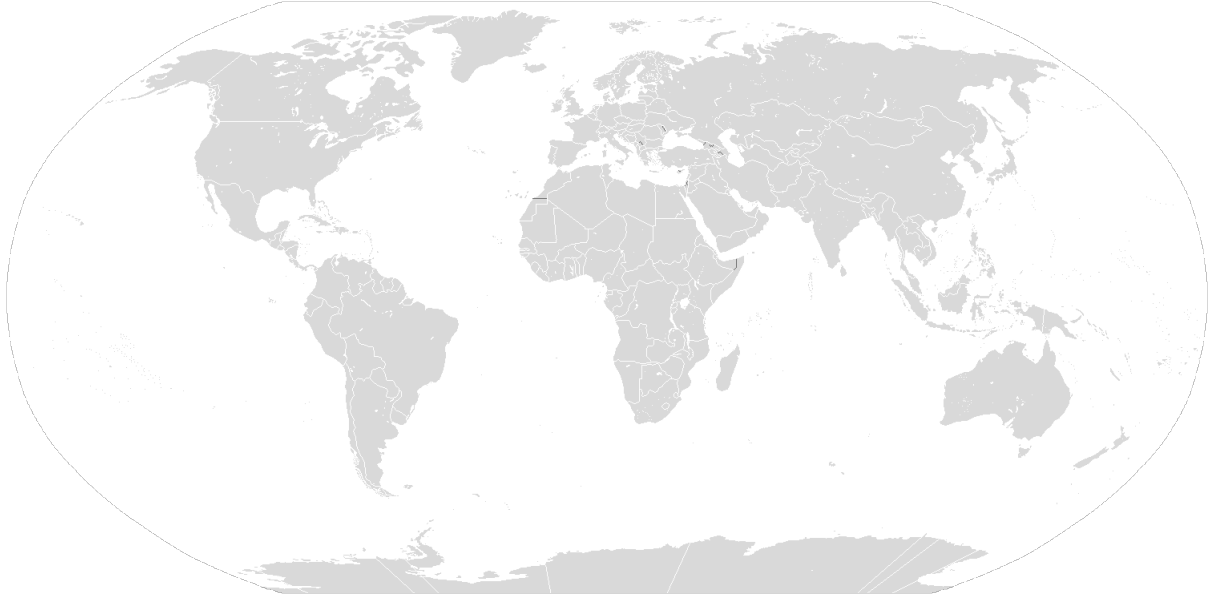


**Figure 3.8:** <change>The figure should be a TS map, but the new TS map has not been generated yet. The previous TS map does not use the best fit parameters, so I have to re-generate the TS map. And this world map is just a reminder and it may be used a lot.</change>

### 3.3.2 PSR J1824.6-2452

The ROI region is a circle whose radius is  $20^\circ$  and all sources outside of  $8^\circ$  are fixed. There are 6 free sources in the region of  $8^\circ$ . The figure 3.9 is a combination of count maps of observation data and the model.

#### Count Maps And Count Cubes

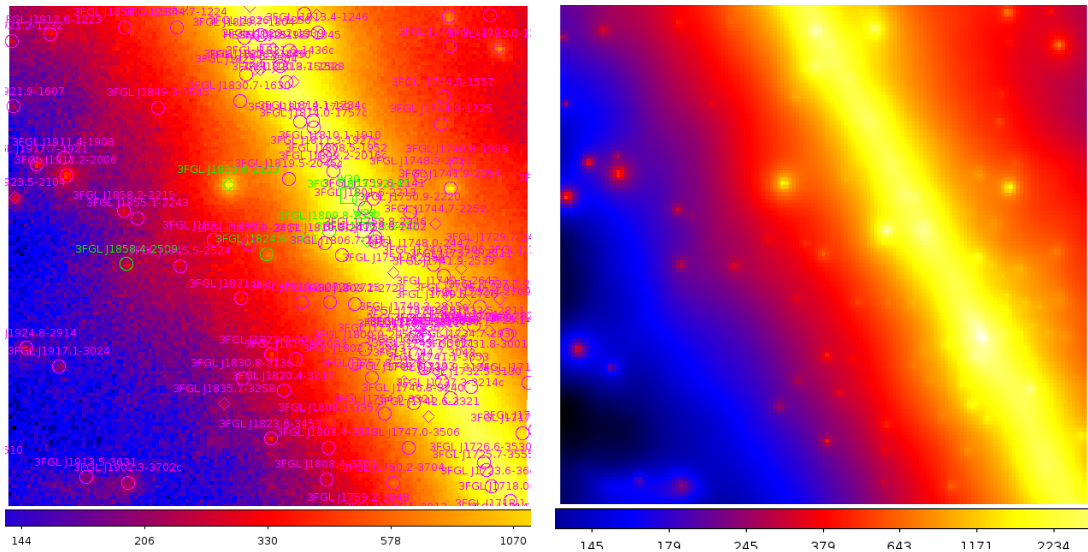


**Figure 3.9:** The count map of PSR J1821.6 (left) and the count map generated by the model. In the left figure, the green circles are free sources while the purple circles are fixed sources. The sizes of the both figures are 141 pixels  $\times$  141 pixels, and each pixel is  $0.2^\circ \times 0.2^\circ$ .

(The figure color bar is a problem. I need to use some other tools to merge the two color bars. Also, I think I should make the color bar be vertical instead of horizontal.)

As the figure 3.9 shown, the PSR J1824.6 is much dimmer than PSR J0218+4232, which implies that the fitting result may be worse. In general, the two figures are quite similar, except that the modeled count map lacks some details and the reason was explained in the previous section 3.3.1.

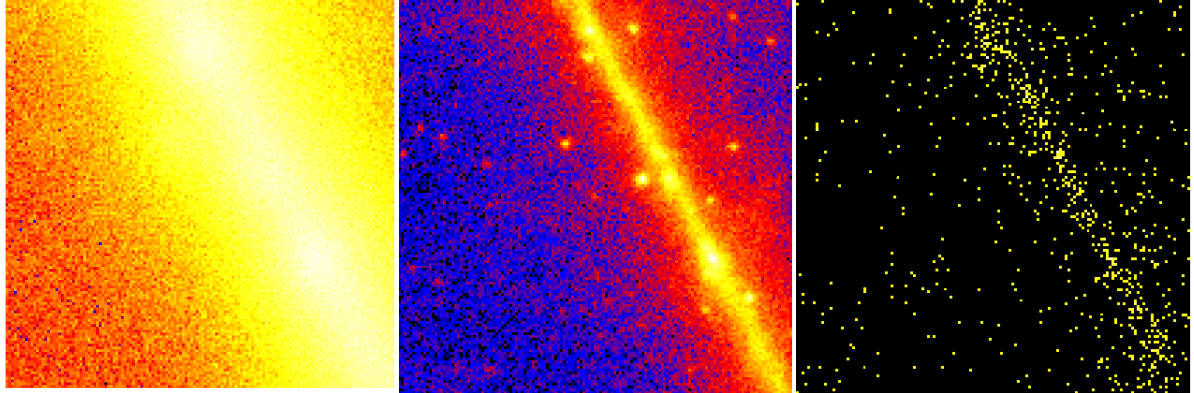


**Figure 3.10:** Three figures of PSR J1824.6's count cube. The energy range of the figure in the left: 100~123MeV, middle: 1.873~2.310GeV, right: 81.11~100GeV.  
 <add>add color bar</add>

The figures 3.10 are count maps of PSR J1824.6-2452 in different energy bands. The target pulsar is too faint in very high energy band and interfered too much by the ambient environment in low energy band (around 100MeV). Because our target source is near the M28 globular cluster and very faint, it is reasonable that the fitting result is worse than PSR J0218+4232.

### Binned Likelihood Analysis

The differences of the count map between the observation data and the model are described as the figure 3.11.

There is an obvious black dot in the figure 3.11 and the value of the dot is large — 1299. The original value from the observation data is 4503. I think the model is acceptable because the source in this pixel is fixed and far away from our target source ( <question>I'm not sure yet.</question> ). So the value of this source does not contribute too much to the center. The values of most other pixels are below 20 implying that the global fit result is acceptable.

The figure 3.12 shows that the global fit is consistent with the flux points generated by fitting sub-energy bins. However, we should notice the first flux points which is denoted as a blue square in the figure 3.12. This flux points is significantly smaller than the global fit (the red line in the figure). What's more, the upper value for the first energy bin is still slightly smaller. <question>I think it is because that the flux points are fitted separately and are independent to the global fit. In fact, we use a single power-lay model to fit each sub-energy bin while PLExpCutoff model to do the global fit. As we have explained previously, the lower energy part of the observation (around 100 MeV) is not reliable. As a result, the separate fit for the first energy bin is not as reliable as the global fit and it is reasonable that the two fitting results are not consistent. When this happens, we have more confidence on the global fit than the separate fit.</question>

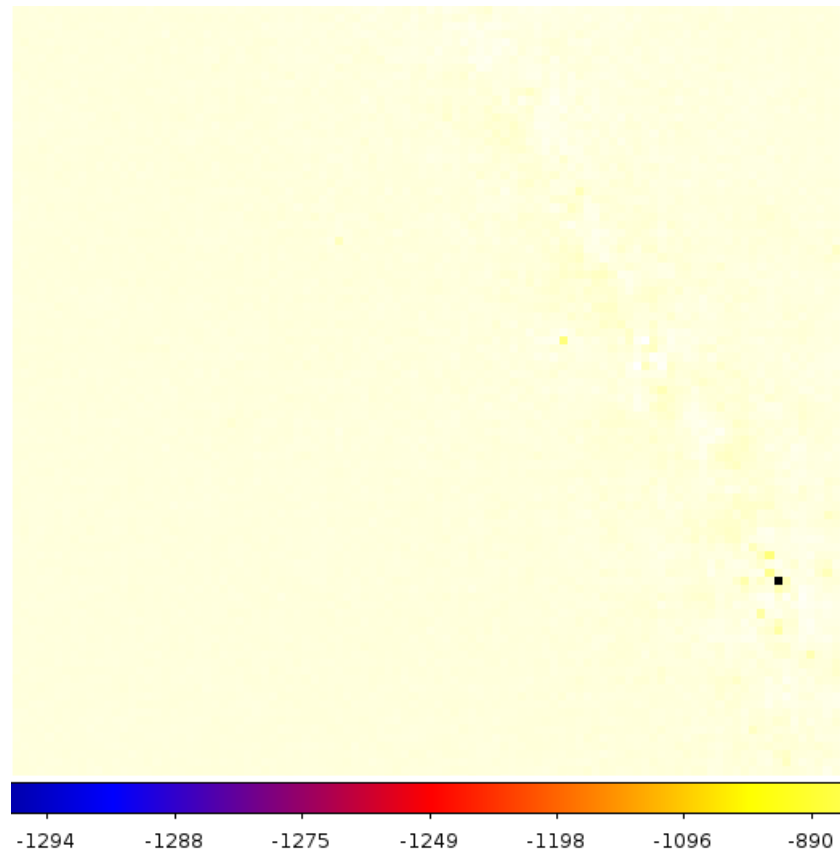


**Figure 3.11:** The residual map shows the difference in photon counts between the observation and the model <change>ugly</change>

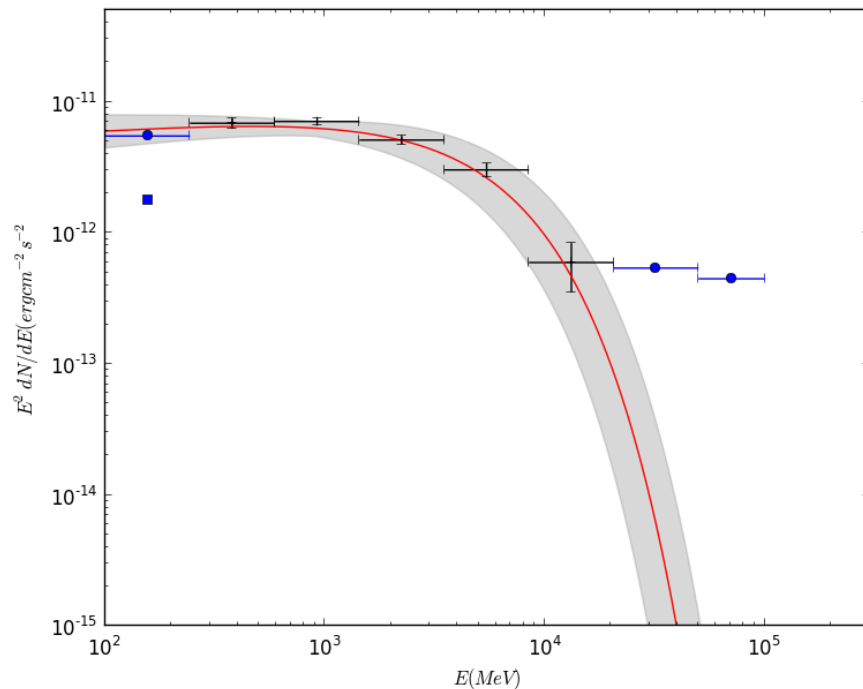


**Figure 3.12:** The log-log plot of flux to energy. <change>should use legends, add arrows for upper values, make the label fonts larger.</change>

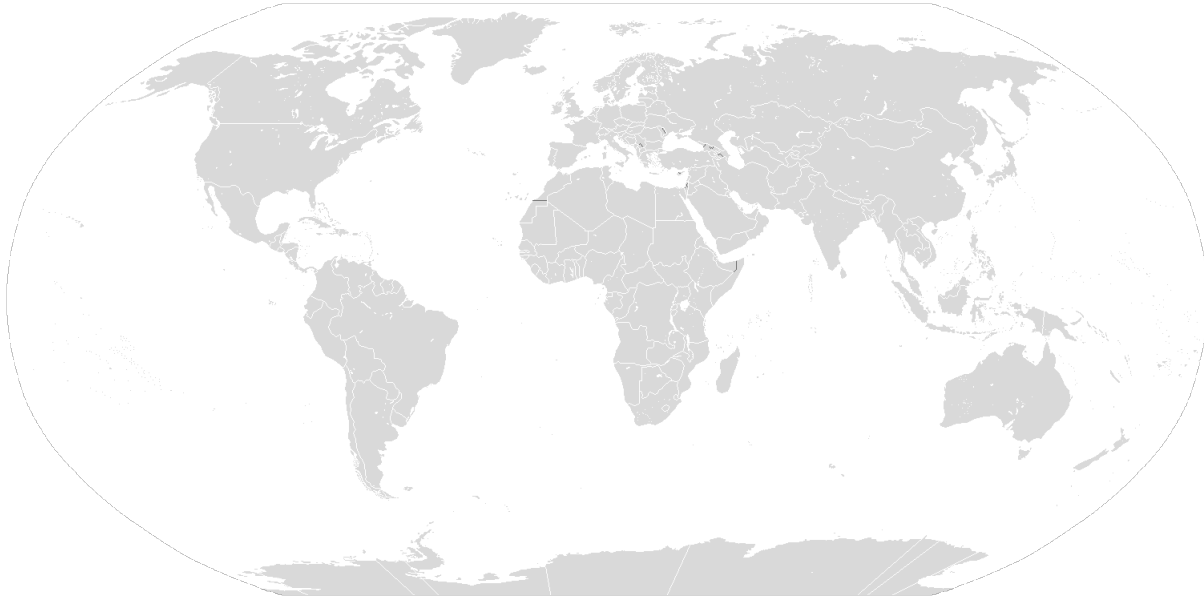


**Figure 3.13:** <*change*>The figure should be a TS map, but the new TS map has not been generated yet. The previous TS map does not use the best fit parameters, so I have to re-generate the TS map. And this world map is just a reminder and it may be used a lot.</*change*>

### 3.3.3 PSR J1939+2134

<**add**>continue here</**add**>